ACS APPLIED MATERIALS & INTERFACES

March 17, 2021
Volume 13
Number 10
pubs.acs.org/acsami

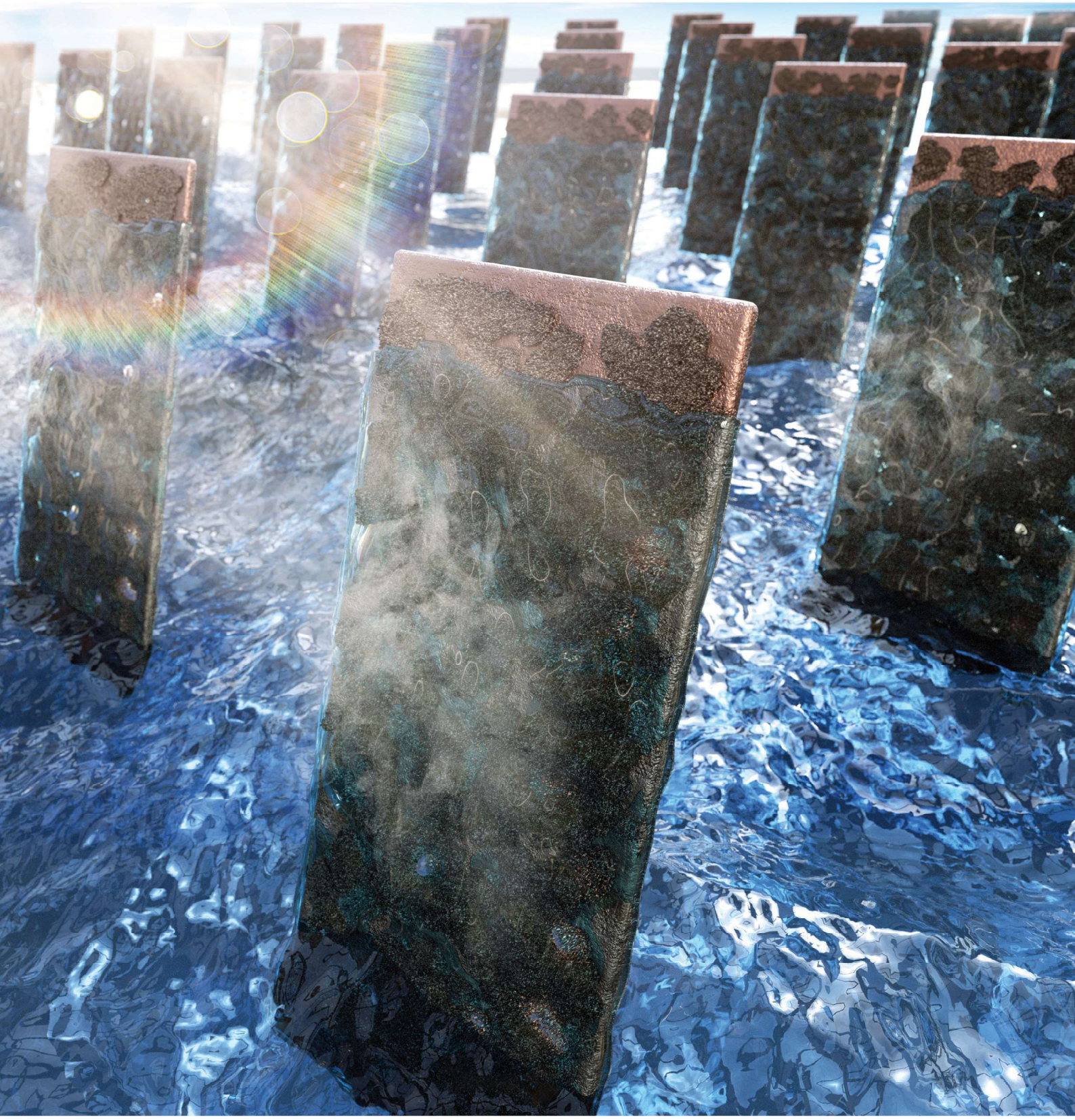

ACS Publications
Most Trusted. Most Cited. Most Read.

www.acs.org

ACS APPLIED MATERIALS & INTERFACES

www.acsami.org

Research Article

Scalable High-Efficiency Bi-Facial Solar Evaporator with a Dendritic Copper Oxide Wick

Jungtaek Kim, Hanseul Choi, Seong Ho Cho, Jaewoo Hwang, Ho-Young Kim,* and Yun Seog Lee*

Cite This: *ACS Appl. Mater. Interfaces* 2021, 13, 11869−11878

Read Online

ACCESS | Metrics & More | Article Recommendations | Supporting Information

ABSTRACT: Solar thermal distillation is a promising way to harvest clean water due to its sustainability. However, the energy density of solar irradiation inevitably demands scalability of the systems. To realize practical applications, it is highly desirable to fabricate meter-scale solar evaporator panels with high capillary performance as well as optical absorptance using scalable and high-throughput fabrication methods. Here, we demonstrate a truly scalable fabrication process for a bi-facial solar evaporator with copper oxide dendrites via the hydrogen bubble templated electrochemical deposition technique. Furthermore, we construct a theoretical model combining capillarity and evaporative mass transfer, which leads to optimal operation conditions and wick characteristics, including superhydrophilicity, extreme capillary performance, and omni-angular high optical absorptance. The fabricated porous surfaces with excellent capillary performance and productivity provide a pathway toward a highly efficient bi-facial solar evaporator panel with meter-level scalability.

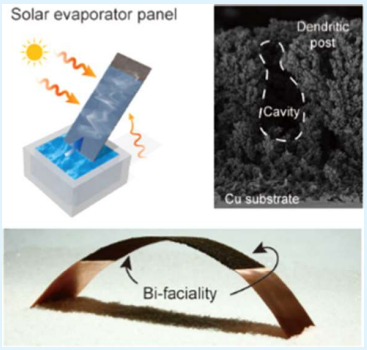

KEYWORDS: *solar evaporator, bi-facial, scalable, electrodeposition, capillary flow*

1. INTRODUCTION

Water scarcity due to climate change has become one of the most important worldwide challenges.[1−3] Various methods have been adopted to produce fresh water, but most of them suffer from environmental sustainability issues mainly arising from use of fossil fuels. On the other hand, solar evaporation-based water distillation or desalination is an environmentally benign and cost-effective method of harvesting clean water.[4] However, to produce 100 L of fresh water per day solely by solar evaporation, an approximately 13.3 square meter-sized panel is required even with an ideal solar energy conversion efficiency of 100%.[4,5] Therefore, to realize a practical solar evaporator, a solar evaporator should be scalable to a meter-level scale while maintaining a high energy conversion efficiency. Since solar evaporation is a phase-change process of water by a radiative heat source, its energy efficiency depends on sunlight absorbance and subsequent heat utilization for water evaporation. However, traditional solar evaporation systems such as solar still have a low efficiency below 50%, due to a high optical reflection at the water surface and significant heat loss through the bulk water and surroundings.[6−8]

Recently, solar evaporators utilizing enhanced mass transfer at the liquid interface on nanometer-scale structures[9,10] have demonstrated significantly improved efficiencies. In those systems, a combination of a porous structure with a high optical absorption surface[11−15] enables highly localized heat generation at the water−air interface,[16−22] thereby minimizing heat losses to bulk water. In particular, solar evaporators with open-channel structures have shown an ideal efficiency of nearly 100% without clogging issues as well as angle adjustability suitable for a solar tracking system.[23] By fabricating a microstructure array on a metal surface, a porous structure and a light-absorbing surface are integrated into a monolithic panel. Since an edge of the panel is in contact with bulk water, the water can be supplied through the capillary surface and the angle of the panel can be adjusted for tracking sun azimuth. Moreover, the open-channel-type solar evaporator can be extended to a bi-facial configuration, which can further harvest additional energy, the albedo, from the rear side of the panel. For a photovoltaic module with a fixed tilt angle, it has been shown that the daily energy generation could be increased up to 130%[24] by using a bi-facial configuration.

However, the previously demonstrated bi-facial solar evaporators are practically limited to centimeter scale due to two major obstacles: salt accumulation and dry-out of the surface. First, salt accumulation impairs the evaporative performance of the interfacial evaporator, in particular, for desalination applications. So far, various solutions for salt accumulation, including natural salt dissolution under cyclic illumination conditions (e.g., day and night) and hierarchical fluid transport network-based fluid convection enhancement to

Received: December 4, 2020
Accepted: February 19, 2021
Published: March 4, 2021

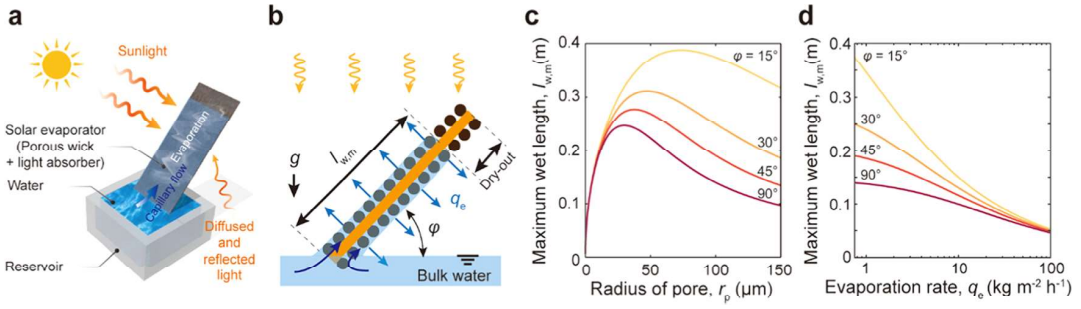

Figure 1. Panel size limits of a bi-facial solar evaporator and the wicking dynamics of water in porous media. (a) Schematic of a solar evaporator panel under evaporation. (b) Schematic of a simplified model for porous capillary rise under gravity and evaporation flux. (c) Maximum rise height vs radius of pore, indicating that the maximum wet length exists at optimal pore size and that the tilt angle decreases the maximum wet length due to the gravitational effect. (d) Maximum wet length vs evaporation rate for various tilt angles.

dilute the high-concentration brine of the evaporation surface before salt precipitation, have been investigated (Figure S1, Supporting Information).[25] Second, the open-channel-type solar evaporator panels intrinsically have an unusable area by dry-out as the panel size increases because the capillary flow of water is significantly limited by gravity and evaporation flux. The dry-out area not only reduces an evaporation area but also allows heat loss to the ambient, which results in lower efficiency. Therefore, it is necessary to fabricate a superwetting surface structure that can wet a square-meter-scale surface area under highly evaporative conditions (e.g., 1−2 kg·m^{-2}·h^{-1} for the 1-Sun illumination condition). In addition, the superwetting surface fabrication process should be high throughput and easily extendable to meter scale. Although there have been various approaches to fabricate porous wick structures for enhancing capillary performance using sintering,[26−28] machining,[29,30] electrochemical processes,[31−34] laser-based machining,[35−37] and photolithography-based microfabrications,[38] the scalability and manufacturing throughput have rarely been explored.

Herein, we describe a highly efficient and scalable bi-facial solar evaporator based on a dendritic copper oxide wick structure using an electrochemical deposition technique[39] combined with surface tension control. To realize a viable bi-facial solar evaporator, there are essential prerequisites including (i) a superhydrophilic surface, (ii) sufficient capillary performance to overcome dry-out, (iii) high and omnidirectional optical absorptance, and (iv) a low-cost fabrication process. Toward a meter-scale solar evaporator panel, we develop a theoretical model for capillary flows on two-dimensional porous surfaces in a bi-facial solar evaporator considering various tilt angles and evaporation conditions. Based on our model, we fabricate superhydrophilic surfaces with nanometer-scale dendritic structures on both sides of a metal plate simultaneously. To prevent dry-out of the panel, we enhance the capillary performance of the surface by generating hydrogen bubbles during the deposition process, which form additional micro-scale capillary channels through copper oxide dendrites. In addition, we show that the hydrogen bubble size can be tailored by adjusting the surface tension of an electrolyte solution and the hydrogen generation rate, which can further improve the capillary performance. This hierarchical structure exhibits extreme scalability compared with the previously reported capillary wicks as well as a high optical absorptance throughout the entire solar spectrum for a wide range of incident angles. By introducing the wick structure into the bi-facial solar evaporator, we demonstrate highly efficient water evaporation that can be extended to a meter-scale level.

2. RESULTS AND DISCUSSION

Dry-out is one of the most critical efficiency-limiting problems of a bi-facial solar evaporator, in particular, with a large panel area. The reduced wet area by dry-out increases the inactive evaporation area with a higher temperature, which increases convective and radiative heat loss. This additional heat loss results in lower energy utilization for water evaporation. As shown in Figure 1a, water from a source at the bottom edge needs to run through the entire surface area under gravitational force and evaporation flux to keep the entire panel surface wet. The capillary imbibition length in typical porous media is often limited to only several centimeters under a typical solar evaporation condition as high as 2 kg·m^{-2}·h^{-1}. Thus, it is important to understand the detailed dynamics of capillary flow in porous media under a high evaporative flux, to prevent dry-out in a large-scale evaporator.

In general, the capillary flow in porous media can be simply described by Darcy's law, where the length of the wetted area (l_w) is a function of time (t), liquid properties including surface tension (γ) and viscosity (μ), and wick structure including permeability (K) and pore size (r_p): $l_w \sim [(4\gamma/\mu)(K/r_p)t]^{1/2}$. Here, the permeability, which quantifies how easily liquids can flow through a porous wick, is proportional to the cross-sectional area of the flow.[40] The capillary flow is also affected by the pore size, r_p. Thus, the ratio of the permeability to pore size, K/r_p, is a key parameter in the wetting performance of a porous wick.

For the capillary flow under gravity and evaporation, the wet length l_w can be described as follows (Figure S2, Supplementary Note S1 and Table S1, Supporting Information)

$$\dot{l}_w = \frac{2\gamma K}{\mu r_p l_w} - \frac{\rho g \sin\varphi K}{\mu} - \frac{q_e}{2\tau} l_w \quad (1)$$

where ρ, φ, q_e, and τ are the liquid density, the tilt angle of the panel, the evaporation flux, and the thickness of the wick structure, respectively. The wet length is converged to the maximum value, $l_{w,m}$, corresponding to $\dot{l}_w = 0$, which determines the largest size of a fully wettable bi-facial evaporator panel under an evaporative condition (Figure 1b). The maximum wet length is a function of tilt angle φ, pore size r_p, and evaporative flux q_e. Figure 1c shows that as the tilt angle of the panel with respect to the water surface gets steeper, $l_{w,m}$ decreases due to the aggravated gravitational effect. However,

https://dx.doi.org/10.1021/acsami.0c21570
ACS Appl. Mater. Interfaces 2021, 13, 11869−11878

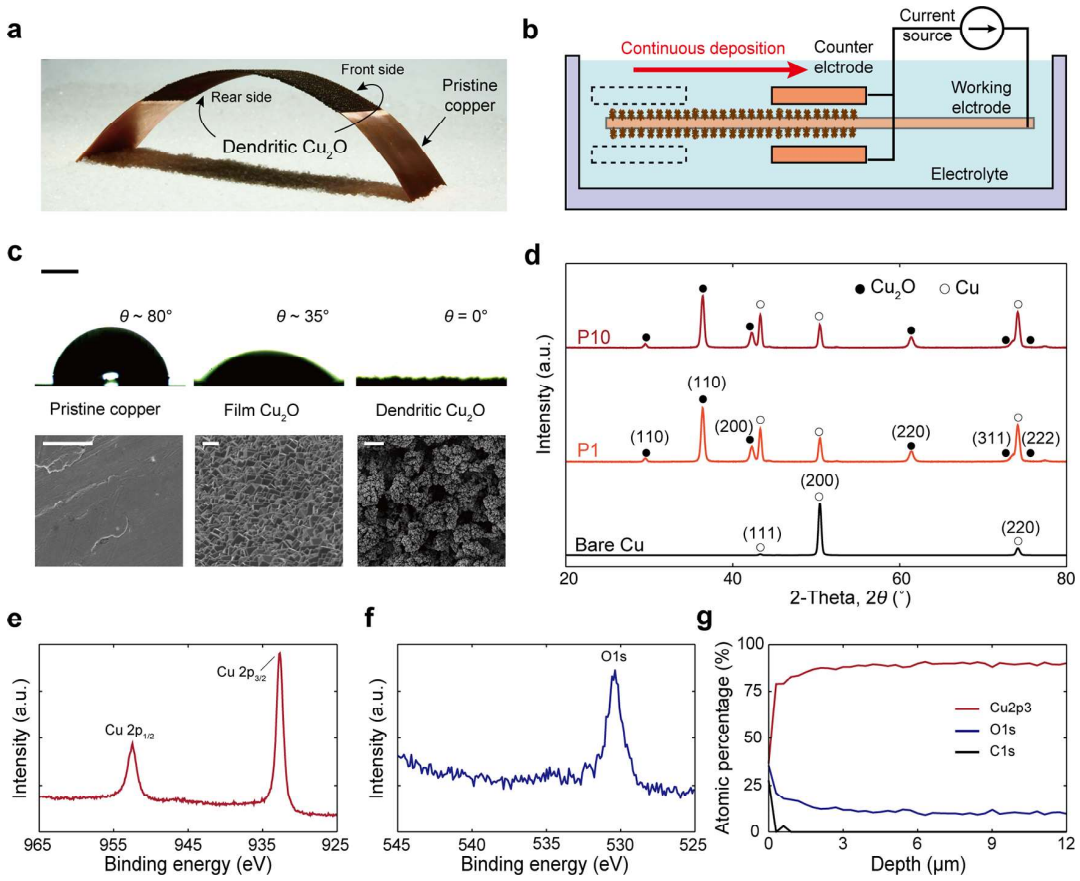

Figure 2. Dendritic copper oxide wick for a bi-facial solar evaporator, and material properties. (a) Bi-facial solar evaporator by hydrogen-templated electrodeposition; both sides of the plate are simultaneously electrodeposited in a single process and the selectively masked area remains intact. (b) Schematic of the electrodeposition setup; bi-faciality can be obtained by electrochemical deposition. A large-size substrate can be coated through continuous plating. (c) Upper row, contact angle of water droplets on pristine copper, continuous copper(I) oxide thin film, and dendritic copper oxide surfaces. The water droplet spreads into dendritic copper oxide within 80 ms, resulting in a contact angle of zero, while the other samples show moderate hydrophilicity. Scale bar, 1 mm. Lower row, SEM images of pristine copper, a continuous copper(I) oxide thin film, and dendritic copper oxide surfaces fabricated by electrochemical deposition. Scale bar, 1 mm, 2 μm, and 100 μm, from left to right. (d) XRD spectra. Crystalline properties of electrochemically deposited dendritic copper oxide samples for 1 min (P1) and 10 min (P10) deposition times and the pristine copper substrate. (e) XPS spectra of a dendritic copper oxide sample for Cu 2p and (f) O 1s. (g) Elemental depth profile of a dendritic copper oxide sample surface measured by XPS by Ar-ion beam sputtering.

for the pore size, there is an optimal value for maximizing the wetted length. As the pore size increases, the flow resistance is reduced due to enlarged conduits. When the pore size becomes excessively large, however, the wet length decreases due to the increased gravitational and evaporation effects. Therefore, the pore size of fabricated copper oxide dendrites should range from 50 to 100 μm for maximized capillary performance (Figure 1c). For a highly evaporative condition under concentrated illumination, the maximum wet length decreases to 0.05 m regardless of the tilt angle (Figure 1d).

We deposit dendritic copper oxide layers on both sides of copper plates to fabricate superhydrophilic surfaces applicable to a bi-facial solar evaporator (Figure 2a). Figure 2b shows a schematic of our electrochemical deposition setup for uniform deposition of copper oxide across a large area by continuous translation of the counter electrode (Figure S3 and Movie S1, Supporting Information). As shown in Figure 2c, an electrochemically deposited copper(I) oxide (Cu_2O) thin film exhibits a lower contact angle (θ) of 35° than pristine copper ($\theta \approx 80°$). To confer superhydrophilicity to the solar evaporator, we further improve the wettability of Cu_2O by using a dendritic growth mode during electrochemical deposition. When applying a current density above 0.05 A·cm^{-2} in the electrolyte solution of the surface tension, γ = 32.2 mN·m^{-1}, we achieved dendritic growth of copper oxide with nanoscale textures as well as porosity. The dendritic copper oxide surface shows superhydrophilicity due to its extreme roughness (Figure 2c).

To investigate the crystal structure and composition of the deposited dendritic copper oxide, we measured X-ray diffraction (XRD) spectra from two deposited samples and a pristine copper substrate, as shown in Figure 2d. We prepared two samples, labeled P1 and P10, which were subjected to copper oxide deposition for 1 and 10 min, respectively, under a current density of 0.05 A·cm^{-2}. The XRD spectra from both samples show peaks matching planes of Cu and Cu_2O (PDF#04-007-9767). The intensities of Cu (111) and (220) peaks of P1 and P10 samples are much higher than those of the bare Cu substrate, implying that the electrochemically deposited structures consist of Cu as well as Cu_2O. To further analyze the elemental composition of the deposited structures, X-ray photoelectron spectroscopy (XPS) was carried out for

https://dx.doi.org/10.1021/acsami.0c21570
ACS Appl. Mater. Interfaces 2021, 13, 11869−11878

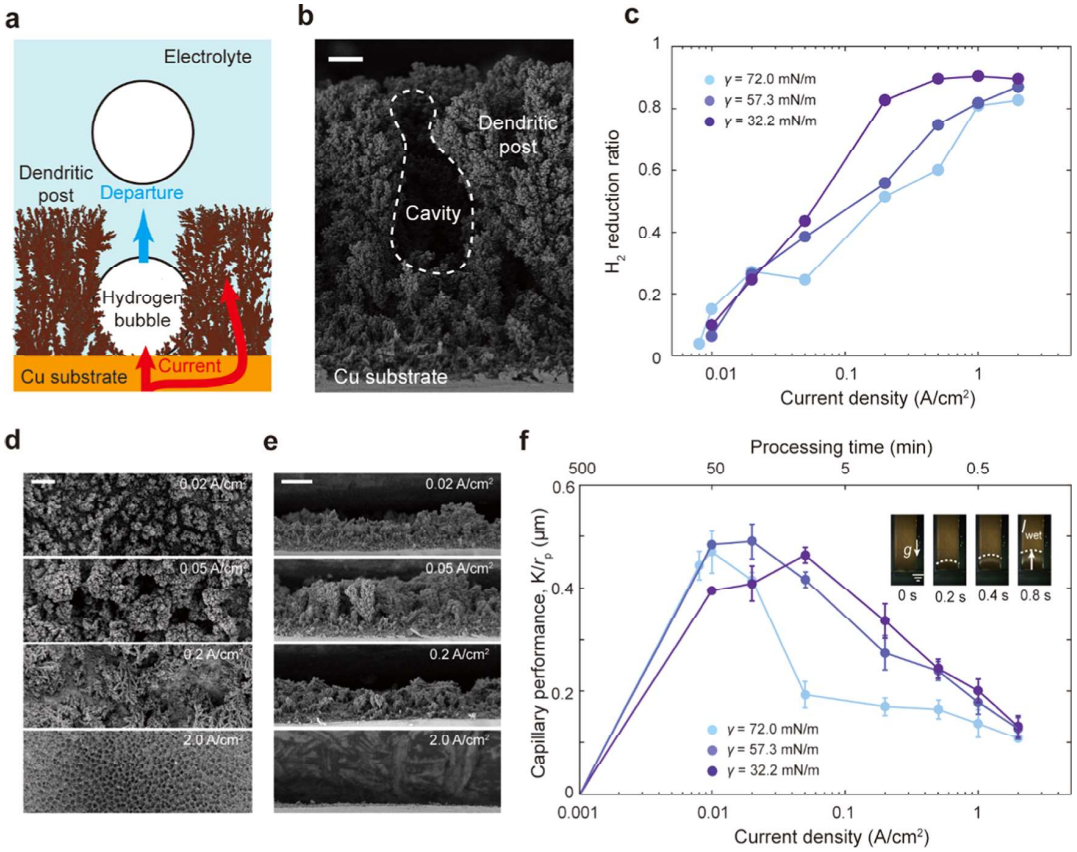

Figure 3. Pore geometry control and capillary performance improvement. (a) Schematic of hydrogen bubble templated electrochemical deposition; hydrogen generation and copper oxide structure deposition occur competitively. Hydrogen bubbles are attached to the surface and prevent the growth of dendritic posts, but detach when they reach a critical size. (b) SEM images of the cross section of fabricated copper oxide dendrites showing a cross-sectional view. Scale bar, 20 μm. (c) Hydrogen reduction ratio vs current density under three different surface tension conditions (γ = 72.0, 57.3, and 32.2 mN·m^{-1}), showing that the reduction rate is mainly affected by current density. (d) SEM images of copper oxide dendrites with various current densities. Scale bar, 100 μm. (e) Cross-sectional view of SEM images with various current densities. Scale bar, 100 μm. (f) Capillary performance vs current density for various surface tension coefficients of the electrolyte solution, indicating that the processing time can be shortened by a factor of 5. Inset, sequential images of capillary rise in the sample deposited for 30 s in a typical aqueous electrolyte solution with a surface tension coefficient of 72 mN·m^{-1}.

the P10 sample (Figure S4, Supporting Information). Figure 2e reveals two main peaks from Cu 2p at 932.3 and 952 eV, and a small satellite peak at 945 eV, confirming the presence of Cu_2O. The O 1s peak can be also observed in Figure 2f. These peaks confirm that our electrochemically deposited surface consists of copper(I) oxide. We also conducted XPS with a depth profiling of the P10 sample by Ar-ion beam sputtering at a sputtering rate of ~0.5 nm·s^{-1} (Figure 2g) to identify the elemental distribution along with the dendrite structures. An oxygen content of O 1s is detected uniformly along with the depth profile after a peak at the top surface, which shows that the oxide layer exists on the entire dendrite layer. The depth profile shows an averaged elemental ratio between copper and oxygen of 86.6:13.4 (Supplementary Note S2, Supporting Information).

Our theoretical model suggests that the pore size of deposited structures should be tailored to 50−100 μm for maximizing the wet length of the evaporator panel. To generate the deterministic micropore size of the structure, we develop a dynamic hydrogen bubble templating method for the electrochemical deposition technique. During the hydrogen-template electroplating, competition between Cu ion reduction and hydrogen gas generation occurs, as illustrated in Figure 3a.[41] While dendritic post structures grow on the substrate under a high current density condition, bubbles are also generated from hydrogen ions in the electrolyte solution and grow on the substrate. In the footprints of grown hydrogen bubbles, copper oxide growth is blocked due to Cu ion depletion, leading to void formation. In the meantime, the copper oxide dendrites grow around hydrogen bubbles and additional hydrogen gas is generated, increasing the size of the bubbles. The hydrogen bubbles grow on the substrate surface until buoyancy exceeds the surface tension force and are detached from the substrate. Here, the critical bubble radius (r_b), the maximum bubble size before the detachment, can be modeled as follows: $r_b \sim [\gamma/(\rho g)]^{1/2}$, where γ is the surface tension coefficient of the electrolyte solution.[42] Despite the bubble detachment, the voids can be repeatedly filled with newly generated hydrogen gas and form pores eventually (Figure 3b). Unlike a pristine copper surface, it can be seen that numerous cavities exist on the electrochemically deposited copper oxide surface (Figure S5, Supporting Information). Thus, the critical bubble radius determines the pore size in the deposited structure, which is the key feature to improve

https://dx.doi.org/10.1021/acsami.0c21570
ACS Appl. Mater. Interfaces 2021, 13, 11869−11878

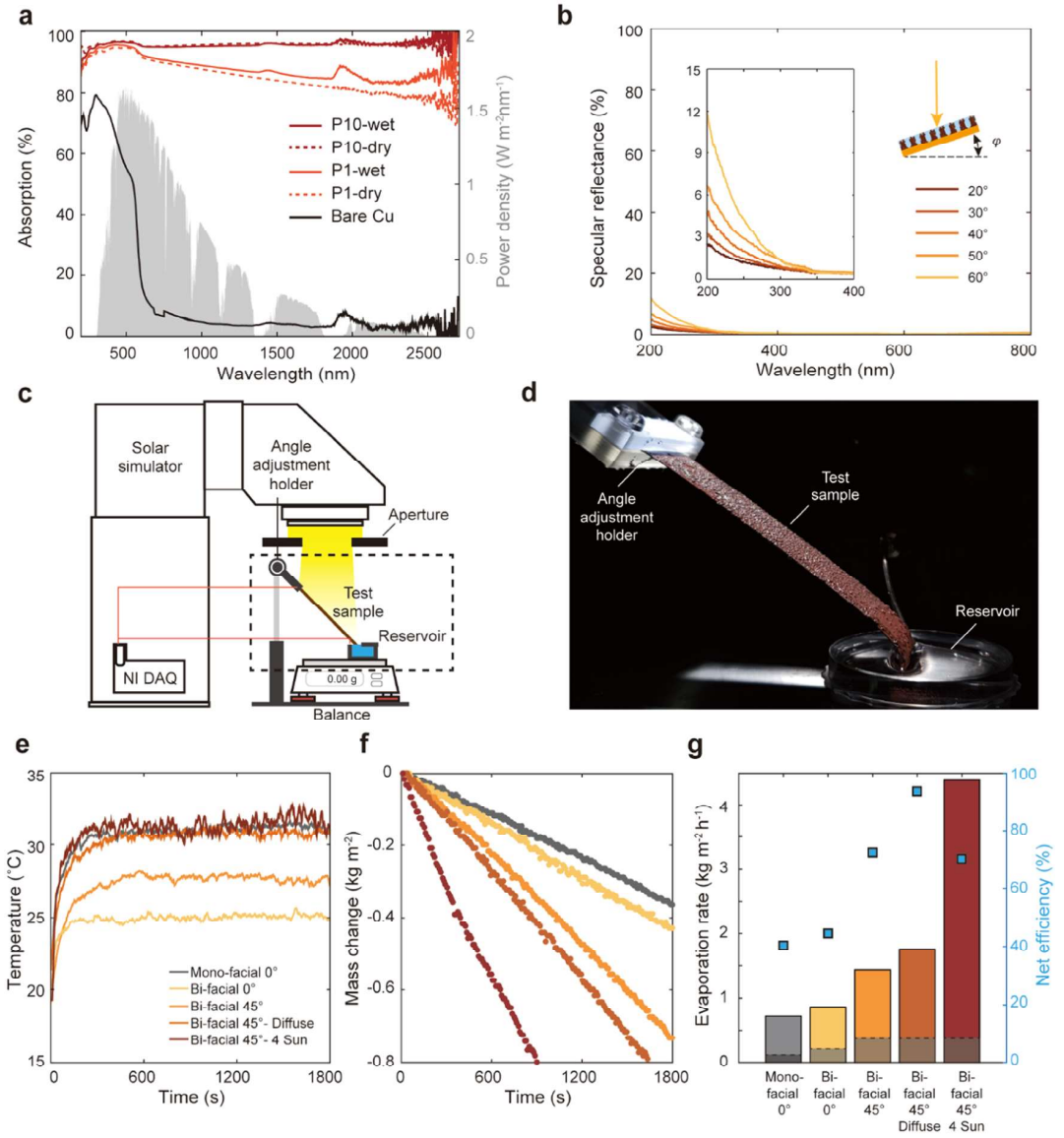

Figure 4. Optical properties of copper oxide dendrites and solar thermal evaporation measurements. (a) Total optical absorptance spectrum of copper oxide dendrite samples under wet (solid lines) and dry (dotted lines) conditions, and a bare copper substrate (black). P1 (orange) and P10 (red) samples indicate 1 and 10 min deposition times, respectively. The AM1.5G solar spectrum is shown in gray color. (b) Absorptance spectrum for various incident angles. (c) Experimental setup for solar evaporation. (d) Photograph of the bi-facial plate with an angle adjustment holder. (e) Temperature of the plate tip vs time. (f) Evaporated water mass over time. (g) Evaporation rate for each sample. The dashed line shows the evaporation rate under dark conditions.

permeability for liquid transport. Since the critical hydrogen bubble radius increases with the current density, $j^{1/3}$, and the surface tension coefficient of the electrolyte,[43] we can control wetting performance by adjusting the current density and the surface tension of the electrolyte solution.

The effect of current density on pore size is investigated by observing hydrogen generation *in situ* with a high-speed camera during the deposition (Figures S6, S7 and Movie S2, Supporting Information) and scanning electron microscopy (SEM) of deposited structures. Also, we estimate the hydrogen reduction rate (Figure 3c), which is defined as $1 - (m_s/m_i)$, where m_s is the mass of the deposited structure. The theoretical mass of a structure without hydrogen generation, m_i, is given by $QM_s/(2F)$, where Q, F, and M_s are the input charge, the Faraday constant, and the molar mass of the structure, respectively. At a low current density, dendritic growth of copper oxide is predominant, and also the hydrogen cavity is distributed randomly between dendritic posts. As the current density increases from 0.008 to 2 A·cm^{-2}, the hydrogen reduction ratio increases from 0.04 to 0.90, so that hydrogen bubbles are more likely to be trapped in the dendritic structure, and cavities are generated while the thickness of the structure increases (Figure 3d,e). In addition, the longitudinal growth of dendrite can be accelerated by concentrating the effective current density with the screening of the hydrogen bubbles. When the current density is higher than 0.05 A·cm^{-2}, the hydrogen reduction ratio becomes excessively large, while the critical bubble radius increases. It also suppresses the growth of

https://dx.doi.org/10.1021/acsami.0c21570
ACS Appl. Mater. Interfaces 2021, 13, 11869−11878

copper oxide dendrites, as the surface is instead covered with a hydrogen bubble layer. The excessive current condition creates an undesirable porous surface for capillary action because the structure becomes too thin with too sparse pores to drive capillary pressure (Figure 3e). Thus, there is an optimum current density that maximizes the longitudinal growth of the structure while creating abundant pores.

The capillary flow performances of the deposited porous structures are measured by the capillary rise height of water through vertically standing structures as shown in Figure 3f. We capture series of sequential images using a high-speed camera at the frame rate of 250 s^{-1} and fit the data to Darcy's law to obtain capillary performance values. For structures deposited under a typical aqueous electrolyte solution with a surface tension coefficient of 72 $mN{\cdot}m^{-1}$, the capillary performance (K/r_p) initially increases as the current density increases from 0 to 0.01 $A{\cdot}cm^{-2}$ and then decreases as the current density increases from 0.01 to 2 $A{\cdot}cm^{-2}$, as shown in Figure 3f. This indicates that the optimal wick structure is formed at the current density of 0.01 $A{\cdot}cm^{-2}$, which balances the competitive generation of copper oxide and hydrogen gas bubbles. However, the optimal current density is relatively low, which needs 50 min to deposit a square meter wick panel. Thus, to achieve a high process throughput, it is desirable to increase the optimal current density without sacrificing the capillary performance.

To overcome the trade-off between the current density and capillary performance, we introduce sodium dodecyl sulfate (SDS) as a surfactant that reduces the surface tension of the electrolyte solution. Since the critical radius of the hydrogen bubble is proportional to 1/2 power of the surface tension coefficient, it is possible to fabricate copper oxide dendritic structures with a high capillary performance under high current density conditions. When the SDS concentrations in the electrolyte solution are 0.01 and 3 mM, the surface tension coefficients are reduced to 57.3 and 32.2 $mN{\cdot}m^{-1}$, respectively (Figure S8, Supporting Information). Samples were prepared by varying the current density and deposition duration while fixing the input total charge under three different surface tension conditions (γ = 72.0, 57.3, and 32.2 $mN{\cdot}m^{-1}$). Reducing the surface tension results in shifting of the conditions for the optimal cavity to 0.05 $A{\cdot}cm^{-2}$, that is, the optimal cavity is created at the higher current density. While the maximum capillary performance values do not decrease significantly, the processing time of plating can be shortened by a factor of 5 thanks to the high current density.

To evaluate the optical absorptance (α) of the deposited structures, UV−Vis−IR spectroscopy was carried out. By using an integrating sphere, we measured the total reflectance (R_t) spectra, the sum of specular and diffuse reflectance, over a wavelength (λ) range between 280 and 2700 nm for the samples to evaluate the optical absorptance, $\alpha(\lambda) = 1 - R_t$. The calculated absorptance spectra of wet and dry electrochemically deposited structures are plotted in Figure 4a. The averaged solar absorptance ($\overline{\alpha}$) can be calculated by $\overline{\alpha} = \int_{280\,nm}^{2700\,nm} \alpha(\lambda)P(\lambda)d\lambda/P_T$, where P_T is the total solar flux and $P(\lambda)$ is the AM1.5G spectral solar power given by the National Renewable Energy Laboratory (NREL). As shown in Figure 4a, the P10 sample exhibits a significantly high averaged solar absorptance of 92.4% compared to that of bare Cu (22.9%). The thicker sample (P10) shows higher averaged solar absorptance, 92.4%, than that of the thinner sample (P1), 88.1%, possibly due to an enhanced re-absorption of reflected photons by dendrite surfaces with the complex geometry. We also measured the optical absorptance of both dry and fully wet surfaces. For the thick sample (P10), the averaged solar absorptance is 92.4 and 92.1% for wet and dry samples, respectively, indicating that the optical reflection by water is minimal.

Since bi-facial solar evaporators need to operate at a tilted angle, we also estimate the incident angle dependency of optical absorptance by measuring specular reflection R_s (λ) at various incident angles without the integrating sphere. As the angle of incidence increases from 20 to 60°, although the reflection tends to increase for a wavelength range below 380 nm, the reflectance is nearly 0% in the visible wavelength range (Figures 4b and S9, Supporting Information). This implies that the tilt angle adjustment of copper oxide dendrites over wide angles would have insignificant effects on solar energy absorption. Hence, our porous structure is highly suitable for the bi-facial solar evaporator with a tilted angle.

To evaluate the performance of the bi-facial solar evaporator based on our porous structures, we deposited a hydrogen bubble templated dendritic copper oxide wick on a 0.3 mm-thick Cu plate (2 × 8.5 cm^2) with mono-facial and bi-facial configurations. The current density and deposition time for all samples were kept the same at 0.05 $A{\cdot}cm^{-2}$ and 10 min, respectively. As shown in Figure 4c, an edge of the solar evaporator was in contact with the free surface of the water reservoir, so that it could imbibe water consistently to compensate for evaporative flow. As a result of the super-hydrophilicity and high capillary performance, the entire surface was kept wet without dry-out (Figure 4d). We measured the amount of evaporated water by the gravimetric method under the 1-Sun illumination condition (1000 $W{\cdot}m^{-2}$) using a class AAA solar simulator exhibiting an intensity increment of less than 4.15% for a 7 cm vertical elevation (Figure S10, Supporting Information). A Fresnel lens was used to create a concentrated (4-Sun) illumination condition. The simulated sunlight was exactly irradiated on the evaporator surface area through an aperture (2 × 8.5 cm^2) installed between the specimen and the light source to calibrate input power. We also adjusted the tilt angle (φ) of the evaporator plate to 0 and 45° by the angle adjustment holder to investigate the role of the rear side evaporation of a bi-facial configuration. For the bi-facial configuration, the aperture was detached in some experimental cases to measure the effect of additional light absorption. During the experiments, the relative humidity was controlled to approximately 50%, and the temperatures of the upper end of the plate, the reservoir, and ambient air were measured simultaneously to determine the thermal loss (Figures 4e and S11, Supporting Information). As shown in Figure 4e, the temperature of the panel rapidly converges to ambient temperature within 600 s.

At a tilt angle of 0°, as shown in Figure 4f,g, the water evaporation rates are measured to be 0.72 and 0.86 $kg{\cdot}m^{-2}{\cdot}h^{-1}$ for mono-facial and bi-facial configurations, respectively, showing an improvement of 21% in the latter system. Heat loss due to convection is inevitable on both sides of the panel. However, if evaporation occurs on both sides, the absorbed heat can be facilitated for evaporation instead of convection loss, increasing the energy efficiency for evaporation. In the case of the bi-facial configuration with a tilt angle of 45°, the evaporation rate further increases to 1.44 $kg{\cdot}m^{-2}{\cdot}h^{-1}$. The evaporation rates under dark conditions, which are indicated by the gray-shaded area in Figure 4g, also show enhanced

https://dx.doi.org/10.1021/acsami.0c21570
ACS Appl. Mater. Interfaces 2021, 13, 11869−11878

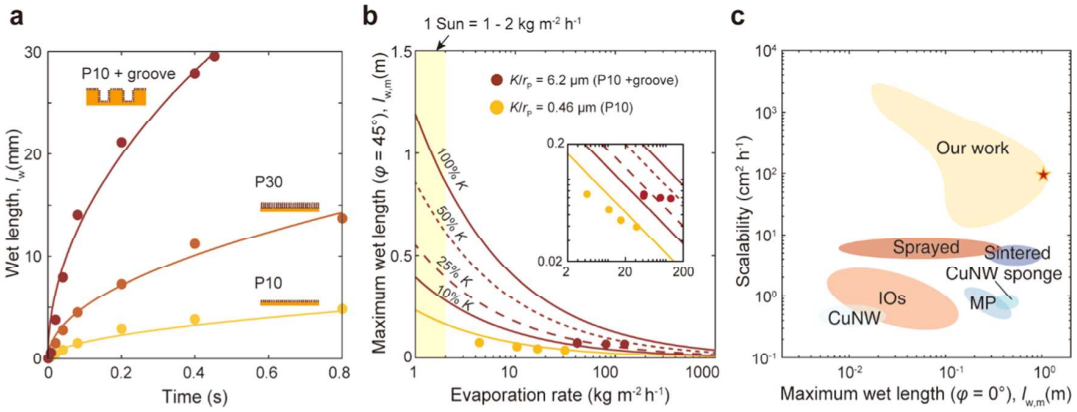

Figure 5. Scalability evaluation of the bi-facial solar evaporator. (a) Wet length vs time with fitting curves based on Darcy's law. The capillary performance of each sample can be obtained from a fitting parameter to match experimental and theoretical results. The sample with macrogrooved copper oxide dendrites shows outstanding capillary performance. (b) Maximum wet length for an extreme condition using electrical heating. Each line based on our theory indicates that our surface can deploy a meter-scale panel for the 1-Sun condition. (c) Comparison of the scalability and the maximum wet length for the current and the conventional fabrication methods. The red star symbol stands for the sample deposited for 10 min on a copper plate with 500 μm wide and 500 μm deep grooves (P10 + groove).

evaporation with a higher tilt angle. This is possibly due to the larger open space at the rear side of the plate, promoting diffusion-limited transport. The energy utilization efficiency of the solar evaporator can be evaluated as follows

$$\eta = (\dot{m}_{e,light} - \dot{m}_{e,dark})h_{fg}/q_s A \cos\varphi \quad (2)$$

where $\dot{m}_{e,light}$ and $\dot{m}_{e,dark}$ are the evaporated water mass rates in illuminating and dark conditions, respectively, h_{fg} is the enthalpy of evaporation, q_s is the solar irradiance, and A is the panel area. Based on the h_{fg} values of bulk water, the solar energy utilization efficiencies for water evaporation of mono-facial 0°, bi-facial 0°, and bi-facial 45° are calculated to be 40.3, 44.5, and 72.4%, respectively. It is noteworthy that the evaporation rates were measured to be 0.12–0.37 kg·m^{-2}·h^{-1} under dark conditions, which should be excluded for the efficiency calculation. We further investigate the merit of additional light harvesting for the bi-facial configuration by removing the aperture so that light can be illuminated onto the surroundings and reflected back to the rear side of the evaporator in a state close to the real operation conditions. By collecting additional energy from diffused and reflected light, the evaporation rate for the bi-facial configuration without the aperture increased to 1.76 kg·m^{-2}·h^{-1}, a relative enhancement of 144% to mono-facial configurations. This bi-facial characteristic was also predicted in the photovoltaic applications, which could increase the daily energy generation in a limited area by up to 30%.[23] In addition, when a concentrated illumination (4-Sun) was used for bi-facial 45°, the evaporation rate increased to 4.54 kg·m^{-2}·h^{-1} without dry-out.

To further elucidate the scalability of the bi-facial solar evaporator, we investigate wet lengths under extremely high evaporation conditions. As shown in Figure 5a, we first measured the capillary rise height to estimate the capillary performance of deposited structures used for the theoretical model by data fitting to Darcy's law. As the deposition time was increased from 10 to 30 min, the wet length at 0.4 s was improved by 3.1 times; however, the productivity, an inverse of the processing time, was decreased by 3 times. To further enhance the capillary performance while maintaining productivity, we deposited structures for 10 min on a copper plate with 500 μm wide and 500 μm deep grooves (P10 + groove), as shown in Figure S5 of the Supporting Information. The grooved sample shows a wet length of 7.91 mm at 0.4 s, which is 8.9 and 2.8 times greater than that of P10 and P30, respectively. In the case of the sample with grooves, the capillary flow resistance is greatly reduced by the macro channel, while the driving force by the micropores is maintained. Thus, the capillary performance value (K/r_p) of P10 with grooves jumps by one order (6.2 μm), compared with that of P10 (0.46 μm) without grooves.

Experiments for measuring dry-out length were conducted by attaching a ceramic heater at the top edge of the 8.5-cm-long evaporator plates fixed with a tilt angle of 45°. As shown in Figure 5b, the wet lengths of samples were measured by a digital imaging technique, while the evaporation rate was controlled across an extremely high evaporation range from 4.336 to 122.8 kg·m^{-2}·h^{-1}, which is equivalent to 3–82 Sun conditions. Based on our model, the maximum wet lengths are also extrapolated to a typical 1-Sun illumination condition (1–2 kg·m^{-2}·h^{-1}). While data of P10 are well matched with our model, the dry-out length of the grooved sample deviates slightly from the model, possibly due to the dry-out along the thickness direction in the groove structure, reducing the effective permeability. We estimate the lower limit of dry-out length assuming that the permeability of the wick is proportional to the cross-sectional area of the liquid stream that is decreased by dry-out. In that case, depending on the permeability, the evaporator surface can stay fully wet and scaled up to a meter for the sample with a capillary performance of 6.2 μm under the 1-Sun condition.

Although various methods for fabricating wick structures have been reported, their scalabilities have not been compared to date. We compare our technique and previous studies in terms of the maximum wet length under the 1-Sun evaporative condition and the process throughput measured by the area that can be fabricated for 1 h (Supplementary Note S3, Table S2, Supporting Information). As can be seen in Figure 5c, the technique in this study exhibits potential for a meter-scale wet length as well as a high process throughput of up to 102 cm^2·h^{-1}. Although the meter-scale wet length can be also realized through a microfabrication or sintering process, their low

https://dx.doi.org/10.1021/acsami.0c21570
ACS Appl. Mater. Interfaces 2021, 13, 11869–11878

process throughputs hinder practical use for meter-scale-level applications.

3. CONCLUSIONS

We have successfully demonstrated a scalable fabrication process of the hydrogen bubble templated dendritic copper oxide wick and its application to a scalable bi-facial solar evaporator. We also have developed a theoretical model of wetting flows in a bi-facial solar evaporator, which yields proper operating conditions and the required capillary performance. The technique based on hydrogen templating electrochemical deposition provides a superhydrophilic surface as well as copper oxide dendrites with suitable capillary performance for a meter-scale device. We have developed a method to tailor micropore geometry by controlling the surface tension of the liquid used in electrodeposition, which does not sacrifice process throughput. The structures also exhibit high optical absorptance independent of the incident angle. This can realize a monolithic panel integrating absorber and evaporation structure for a bi-facial solar evaporator effective in a range of tilt angles. The angle adjustment has great advantages of setting suitable altitudes, and the reflected light incident to the backside can be harvested when it is deployed in the field. By implementing a bi-facial configuration, the solar evaporation measurement under a simulated 1-Sun illumination condition shows a water evaporation rate of up to 1.76 $kg{\cdot}m^{-2}{\cdot}h^{-1}$, indicating a high evaporation efficiency as well as the advantage of absorption of additional light from the surroundings. Furthermore, from the dry-out characteristics under extremely high evaporation conditions, the demonstrated capillary performance and the high process throughput are estimated to obtain a highly efficient bi-facial solar evaporator of a meter scale.

4. EXPERIMENTAL SECTION

4.1. Electrochemical Deposition of Copper Oxide Dendrites. The aqueous electrolyte solution contains 0.1 M $CuSO_4$ and 0.5 M H_2SO_4. To control the surface tension of the solution, sodium dodecyl sulfate was added at concentrations of 0.01 and 3 mM. The force tensiometer (K100, Kruss) was used to measure the surface tension of the electrolyte with the Wilhelmy plate method. Before deposition, copper substrates and electrodes were cleaned with ethanol, dilute HCl (1 M), and de-ionized water. Both the working and counter electrodes are made of copper, and a constant current density was supplied by a DC power supply (PWS2326, Tektronix). After electrodeposition, the samples were immersed in DI water to rinse the residue and dried in ambient air.

4.2. Porous Structure Characterization and Visualization. The capillary performance measurement setup consists of a high-speed camera (SA 1.1, Photron), an LED light (Cyclops I, KOMI), and optomechanical components (Thorlabs). The sample was fixed on an optomechanical beam perpendicular to the liquid interface. To measure the wet length as a function of time, the reservoir was slowly elevated by a z-stage to make the sample come into contact with liquid and time-sequential images were recorded with a high-speed camera. The capillary performance of each sample was obtained from a fitting parameter to match experimental and theoretical results based on Darcy's law. The hydrogen bubble generation was recorded as shown in Figure S6. SEM imaging was performed with a field-emission scanning electron microscope (SUPRA 55VP, Carl Zeiss).

4.3. Characterization of Materials. The total reflectance of samples was measured by an ultraviolet−visible−infrared (UV−Vis−IR) spectrometer (V-770, JASCO) equipped with an integrating sphere. Specular reflectance of the samples was measured with a UV−Vis−IR spectrometer (Cary 5000, Varian) equipped with a Cary various-angle specular reflectance accessory in the 200−800 nm region. All samples were measured in dry and wet conditions in sequence, by dropping a few drops of de-ionized water at the surfaces. The structural properties were measured by an X'Pert PRO (PANalytical), with a Cu Kα radiation source operated at an accelerating voltage of 40 kV with a current of 30 mA. Samples were scanned by θ−2θ mode. The elemental composition was measured by X-ray photoelectron spectroscopy (Nexsa, Thermofisher Scientific) with an Ar-ion source at 2 kV.

4.4. Solar Simulator. The solar evaporator performance was measured with a xenon-arc lamp-based solar simulator (Newport Oriel Sol3A, 94043A-1000) under 1-Sun illumination (100 $mW{\cdot}cm^{-2}$) with an AM1.5G filter. The illumination intensity was calibrated using a Si-reference cell certified by NREL (Supplementary Note S4).

4.5. Evaporation Performance Test. The evaporation rate was measured by the gravimetric method under the 1-Sun illumination condition. The upper side of the sample was gripped by a 3D-printed fixture that was placed outside of the balance. The lower side of the sample was in contact with the water surface in a reservoir to keep the entire surface wet. The evaporation rate is equal to the rate of the decreased mass of the reservoir placed on the balance owing to the sample imbibing water continuously to compensate for evaporated water.

■ ASSOCIATED CONTENT

Supporting Information

The Supporting Information is available free of charge at https://pubs.acs.org/doi/10.1021/acsami.0c21570.

Cyclic test for simulated seawater (3.5 wt % NaCl); schematic diagram of capillary flow in porous media under gravitational and evaporation effects; continuous electrodeposition for meter-scale, XPS spectra of the copper oxide dendrite sample; SEM images of copper surfaces with various treatment processes; bubble visualization setup; effect of bubble generation on pore structure; surface tension coefficient of the electrolyte solution depending on the concentration of the added surfactant (SDS, sodium dodecyl sulfate); total reflectance spectra for various incident angles using an integrating sphere; schematic of the solar evaporation test and an illumination intensity profile; temperature of reservoir vs evaporation time; evaporative capillary rise model and parameters; estimation of copper and copper oxide ratio; comparison of capillary performance for estimation of wet length; optical absorption efficiency calculation; physics of evaporation: heat and mass-transfer analysis for the solar interfacial evaporator; feasibility test for the issue of salt accumulation in solar desalination; cost estimation of the dendritic copper oxide wick and comparison; and comparison of evaporation performance (PDF)

Continuous electrodeposition (Movie S1) (MP4)

Visualization of hydrogen bubble generation (Movie S2) (MP4)

■ AUTHOR INFORMATION

Corresponding Authors

Ho-Young Kim − *Department of Mechanical Engineering, Seoul National University, Seoul 08826, Republic of Korea*; Email: hyk@snu.ac.kr

Yun Seog Lee − *Department of Mechanical Engineering and Inter-University Semiconductor Research Center, Seoul National University, Seoul 08826, Republic of Korea;*

https://dx.doi.org/10.1021/acsami.0c21570
ACS Appl. Mater. Interfaces 2021, 13, 11869−11878

orcid.org/0000-0002-2289-109X; Email: leeyunseog@snu.ac.kr

Authors

Jungtaek Kim − *Department of Mechanical Engineering, Seoul National University, Seoul 08826, Republic of Korea*

Hanseul Choi − *Department of Mechanical Engineering, Seoul National University, Seoul 08826, Republic of Korea*

Seong Ho Cho − *Department of Mechanical Engineering, Seoul National University, Seoul 08826, Republic of Korea*

Jaewoo Hwang − *Department of Mechanical Engineering, Seoul National University, Seoul 08826, Republic of Korea*

Complete contact information is available at: https://pubs.acs.org/10.1021/acsami.0c21570

Author Contributions

This manuscript was written through contributions of all authors. All authors have given approval to the final version of the manuscript. J.H. participated in the revision process for evaporation heat transfer analysis.

Notes

The authors declare no competing financial interest.

■ ACKNOWLEDGMENTS

This work was supported by the New Faculty Startup Fund from Seoul National University (SNU), the Ministry of Trade, Industry and Energy of Korea (Grant No. 2018-20000187), and the National Research Foundation of Korea (Grant Nos. 2018-052541 and 2020R1C1C1005880) via SNU-IAMD and the Institute of Engineering Research.

■ REFERENCES

(1) Schewe, J.; Heinke, J.; Gerten, D.; Haddeland, I.; Arnell, N. W.; Clark, D. B.; Dankers, R.; Eisner, S.; Fekete, B. M.; Colón-González, F. J.; Gosling, S. N.; Kim, H.; Liu, X.; Masaki, Y.; Portmann, F. T.; Satoh, Y.; Stacke, T.; Tang, Q.; Wada, Y.; Wisser, D.; Albrecht, T.; Frieler, K.; Piontek, F.; Warszawski, L.; Kabat, P. Multimodel Assessment of Water Scarcity under Climate Change. *Proc. Natl. Acad. Sci. U.S.A.* **2014**, *111*, 3245−3250.

(2) Shannon, M. A.; Bohn, P. W.; Elimelech, M.; Georgiadis, J. G.; Mariñas, B. J.; Mayes, A. M. Science and Technology for Water Purification in the Coming Decades. *Nature* **2008**, *452*, 301−310.

(3) Li, C.; Goswami, Y.; Stefanakos, E. Solar Assisted Sea Water Desalination: A Review. *Renewable Sustainable Energy Rev.* **2013**, *19*, 136−163.

(4) Qiblawey, H. M.; Banat, F. Solar Thermal Desalination Technologies. *Desalination* **2008**, *220*, 633−644.

(5) Crabtree, G. W.; Lewis, N. S. Solar Energy Conversion. *Phys. Today* **2007**, *60*, 37−42.

(6) Dsilva Winfred Rufuss, D.; Iniyan, S.; Suganthi, L.; Davies, P. A. Solar Stills: A Comprehensive Review of Designs, Performance and Material Advances. *Renewable Sustainable Energy Rev.* **2016**, *63*, 464−496.

(7) Kabeel, A. E.; El-Agouz, S. A. Review of Researches and Developments on Solar Stills. *Desalination* **2011**, *276*, 1−12.

(8) Chen, C.; Kuang, Y.; Hu, L. Challenges and Opportunities for Solar Evaporation. *Joule* **2019**, *3*, 683−718.

(9) Wang, Z.; Liu, Y.; Tao, P.; Shen, Q.; Yi, N.; Zhang, F.; Liu, Q.; Song, C.; Zhang, D.; Shang, W.; Deng, T. Bio-Inspired Evaporation Through Plasmonic Film of Nanoparticles at the Air−Water Interface. *Small* **2014**, *10*, 3234−3239.

(10) Ghasemi, H.; Ni, G.; Marconnet, A. M.; Loomis, J.; Yerci, S.; Miljkovic, N.; Chen, G. Solar Steam Generation by Heat Localization. *Nat. Commun.* **2014**, *5*, No. 4449.

(11) Zhou, L.; Tan, Y.; Wang, J.; Xu, W.; Yuan, Y.; Cai, W.; Zhu, S.; Zhu, J. 3D Self-Assembly of Aluminium Nanoparticles for Plasmon-Enhanced Solar Desalination. *Nat. Photonics* **2016**, *10*, 393−398.

(12) Wang, J.; Li, Y.; Deng, L.; Wei, N.; Weng, Y.; Dong, S.; Qi, D.; Qiu, J.; Chen, X.; Wu, T. High-Performance Photothermal Conversion of Narrow-Bandgap Ti2O3 Nanoparticles. *Adv. Mater.* **2017**, *29*, No. 1603730.

(13) Liu, H.; Chen, C.; Wen, H.; Guo, R.; Williams, N. A.; Wang, B.; Chen, F.; Hu, L. Narrow Bandgap Semiconductor Decorated Wood Membrane for High-Efficiency Solar-Assisted Water Purification. *J. Mater. Chem. A* **2018**, *6*, 18839−18846.

(14) Li, Y.; Gao, T.; Yang, Z.; Chen, C.; Luo, W.; Song, J.; Hitz, E.; Jia, C.; Zhou, Y.; Liu, B.; Yang, B.; Hu, L. 3D-Printed, All-in-One Evaporator for High-Efficiency Solar Steam Generation under 1 Sun Illumination. *Adv. Mater.* **2017**, *29*, No. 1700981.

(15) Zhou, L.; Tan, Y.; Ji, D.; Zhu, B.; Zhang, P.; Xu, J.; Gan, Q.; Yu, Z.; Zhu, J. Self-Assembly of Highly Efficient, Broadband Plasmonic Absorbers for Solar Steam Generation. *Sci. Adv.* **2016**, *2*, No. e1501227.

(16) Ni, G.; Li, G.; Boriskina, S. V.; Li, H.; Yang, W.; Zhang, T.; Chen, G. Steam Generation under One Sun Enabled by a Floating Structure with Thermal Concentration. *Nat. Energy* **2016**, *1*, 16126.

(17) Cooper, T. A.; Zandavi, S. H.; Ni, G. W.; Tsurimaki, Y.; Huang, Y.; Boriskina, S. V.; Chen, G. Contactless Steam Generation and Superheating under One Sun Illumination. *Nat. Commun.* **2018**, *9*, No. 5086.

(18) Xu, N.; Li, J.; Wang, Y.; Fang, C.; Li, X.; Wang, Y.; Zhou, L.; Zhu, B.; Wu, Z.; Zhu, S.; Zhu, J. A Water Lily−Inspired Hierarchical Design for Stable and Efficient Solar Evaporation of High-Salinity Brine. *Sci. Adv.* **2019**, *5*, No. eaaw7013.

(19) Li, C.; Jiang, D.; Huo, B.; Ding, M.; Huang, C.; Jia, D.; Li, H.; Liu, C.-Y.; Liu, J. Scalable and Robust Bilayer Polymer Foams for Highly Efficient and Stable Solar Desalination. *Nano Energy* **2019**, *60*, 841−849.

(20) Liu, P.-F.; Miao, L.; Deng, Z.; Zhou, J.; Su, H.; Sun, L.; Tanemura, S.; Cao, W.; Jiang, F.; Zhao, L.-D. A Mimetic Transpiration System for Record High Conversion Efficiency in Solar Steam Generator Under One-Sun. *Mater. Today Energy* **2018**, *8*, 166−173.

(21) Xue, G.; Liu, K.; Chen, Q.; Yang, P.; Li, J.; Ding, T.; Duan, J.; Qi, B.; Zhou, J. Robust and Low-Cost Flame-Treated Wood for High-Performance Solar Steam Generation. *ACS Appl. Mater. Interfaces* **2017**, *9*, 15052−15057.

(22) Wang, K.; Huo, B.; Liu, F.; Zheng, Y.; Zhang, M.; Cui, L.; Liu, J. In Situ Generation of Carbonized Polyaniline Nanowires on Thermally-Treated and Electrochemically-Etched Carbon Fiber Cloth for High Efficient Solar Seawater Desalination. *Desalination* **2020**, *481*, No. 114303.

(23) Singh, S. C.; ElKabbash, M.; Li, Z.; Li, X.; Regmi, B.; Madsen, M.; Jalil, S. A.; Zhan, Z.; Zhang, J.; Guo, C. Solar-Trackable Super-Wicking Black Metal Panel for Photothermal Water Sanitation. *Nat. Sustainability* **2020**, *3*, 938−946.

(24) Kopecek, R.; Libal, J. Towards Large-Scale Deployment of Bifacial Photovoltaics. *Nat. Energy* **2018**, *3*, 443−446.

(25) Zhang, Y.; Xiong, T.; Nandakumar, D. K.; Tan, S. C. Structure Architecting for Salt-Rejecting Solar Interfacial Desalination to Achieve High-Performance Evaporation With In Situ Energy Generation. *Adv. Sci.* **2020**, *7*, No. 1903478.

(26) Deng, D.; Liang, D.; Tang, Y.; Peng, J.; Han, X.; Pan, M. Evaluation of Capillary Performance of Sintered Porous Wicks for Loop Heat Pipe. *Exp. Therm. Fluid Sci.* **2013**, *50*, 1−9.

(27) Deng, D.; Tang, Y.; Huang, G.; Lu, L.; Yuan, D. Characterization of Capillary Performance of Composite Wicks for Two-Phase Heat Transfer Devices. *Int. J. Heat Mass Transfer* **2013**, *56*, 283−293.

(28) Holley, B.; Faghri, A. Permeability and Effective Pore Radius Measurements for Heat Pipe and Fuel Cell Applications. *Appl. Therm. Eng.* **2006**, *26*, 448−462.

(29) Huang, G.; Yuan, W.; Tang, Y.; Zhang; Zhang, S.; Lu, L. Enhanced Capillary Performance in Axially Grooved Aluminium

Wicks by Alkaline Corrosion Treatment. *Exp. Therm. Fluid Sci.* **2017**, *82*, 212−221.
(30) Zhang, S.; Lin, L.; Chen, G.; Tang, H.; Zeng, J.; Yuan, W.; Tang, Y. Experimental Study on the Capillary Performance of Aluminum Micro-Grooved Wicks with Reentrant Cavity Array. *Int. J. Heat Mass Transfer* **2019**, *139*, 917−927.
(31) Zhang, C.; Lingamneni, S.; Barako, M. T.; Palko, J. W.; Asheghi, M.; Goodson, K. E. In *Characterization of The Capillary Performance of Copper Inverse Opals*, 2016 15th IEEE Intersociety Conference on Thermal and Thermomechanical Phenomena in Electronic Systems (ITherm), 31 May−3 June, 2016; pp 1035−1039.
(32) Zhang, C.; Palko, J. W.; Barako, M. T.; Asheghi, M.; Santiago, J. G.; Goodson, K. E. Enhanced Capillary-Fed Boiling in Copper Inverse Opals via Template Sintering. *Adv. Funct. Mater.* **2018**, *28*, No. 1803689.
(33) Lee, J.; Suh, Y.; Dubey, P. P.; Barako, M. T.; Won, Y. Capillary Wicking in Hierarchically Textured Copper Nanowire Arrays. *ACS Appl. Mater. Interfaces* **2019**, *11*, 1546−1554.
(34) Jung, S. M.; Preston, D. J.; Jung, H. Y.; Deng, Z.; Wang, E. N.; Kong, J. Porous Cu Nanowire Aerosponges from One-Step Assembly and their Applications in Heat Dissipation. *Adv. Mater.* **2016**, *28*, 1413−1419.
(35) Vorobyev, A. Y.; Guo, C. Laser Turns Silicon Superwicking. *Opt. Express* **2010**, *18*, 6455−6460.
(36) Vorobyev, A. Y.; Guo, C. Metal Pumps Liquid Uphill. *Appl. Phys. Lett.* **2009**, *94*, No. 224102.
(37) Ngo, C.-V.; Chun, D.-M. Control of Laser-Ablated Aluminum Surface Wettability to Superhydrophobic or Superhydrophilic through Simple Heat Treatment or Water Boiling Post-Processing. *Appl. Surf. Sci.* **2018**, *435*, 974−982.
(38) Nam, Y.; Sharratt, S.; Byon, C.; Kim, S. J.; Ju, Y. S. Fabrication and Characterization of the Capillary Performance of Superhydrophilic Cu Micropost Arrays. *J. Microelectromech. Syst.* **2010**, *19*, 581−588.
(39) Plowman, B. J.; Jones, L. A.; Bhargava, S. K. Building with Bubbles: the Formation of High Surface Area Honeycomb-Like Films via Hydrogen Bubble Templated Electrodeposition. *Chem. Commun.* **2015**, *51*, 4331−4346.
(40) Ha, J.; Kim, H.-Y. Capillarity in Soft Porous Solids. *Annu. Rev. Fluid Mech.* **2020**, *52*, 263−284.
(41) Li, S.; Furberg, R.; Toprak, M. S.; Palm, B.; Muhammed, M. Nature-Inspired Boiling Enhancement by Novel Nanostructured Macroporous Surfaces. *Adv. Funct. Mater.* **2008**, *18*, 2215−2220.
(42) Cole, R. Bubble Frequencies and Departure Volumes at Subatmospheric Pressures. *AlChE J.* **1967**, *13*, 779−783.
(43) Fernández, D.; Maurer, P.; Martine, M.; Coey, J. M. D.; Möbius, M. E. Bubble Formation at a Gas-Evolving Microelectrode. *Langmuir* **2014**, *30*, 13065−13074.

https://dx.doi.org/10.1021/acsami.0c21570
ACS Appl. Mater. Interfaces 2021, 13, 11869−11878

Supporting Information

Scalable High-Efficiency Bi-Facial Solar Evaporator with a Dendritic Copper Oxide Wick

Jungtaek Kim[†], *Hanseul Choi*[†], *Seong Ho Cho*[†], *Jaewoo Hwang*[†],

Ho-Young Kim[*,†] *and Yun Seog Lee*[*,†,‡]

† Department of Mechanical Engineering, Seoul National University, Seoul 08826, Republic of Korea

‡ Inter-University Semiconductor Research Center, Seoul National University, Seoul 08826, Republic of Korea

*Corresponding authors

Ho-Young Kim: hyk@snu.ac.kr

Yun Seog Lee: leeyunseog@snu.ac.kr

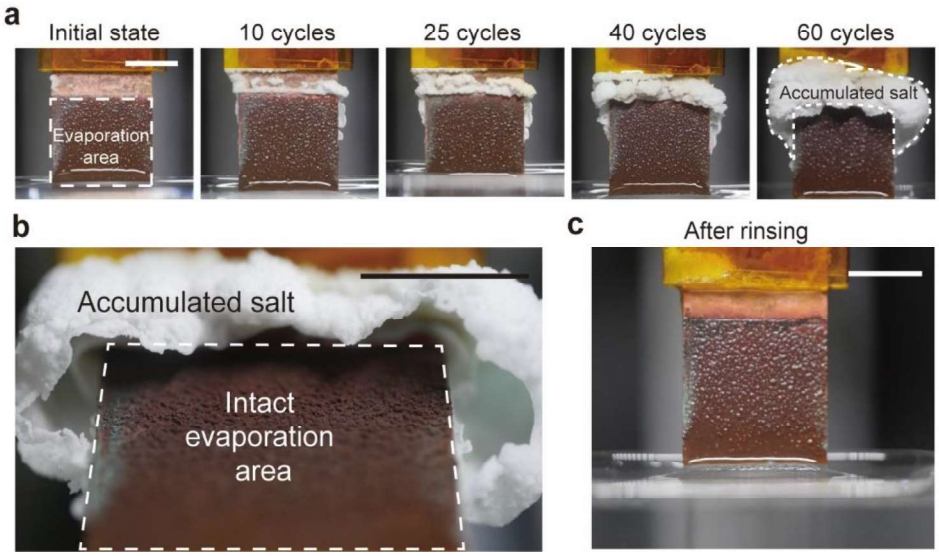

Figure S1. Cyclic test for simulated seawater (3.5 wt % NaCl). (a) Sequential images of devices throughout 60-cycle-test. (b) A magnified image of accumulated salt structure. Salt structures grow only at the edge while the evaporation area intact. (c) Rinsed sample by simulated sea water. The accumulated salt is simply dissolved and the sample is restored to initial state. Scale bar, 10 mm.

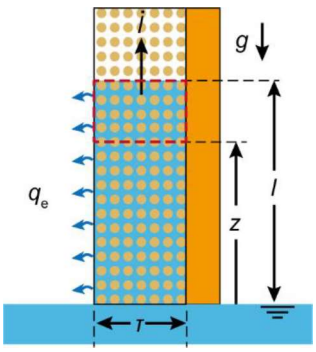

Figure S2. Schematic diagram of capillary flow in porous media under gravitational and evaporation effects.

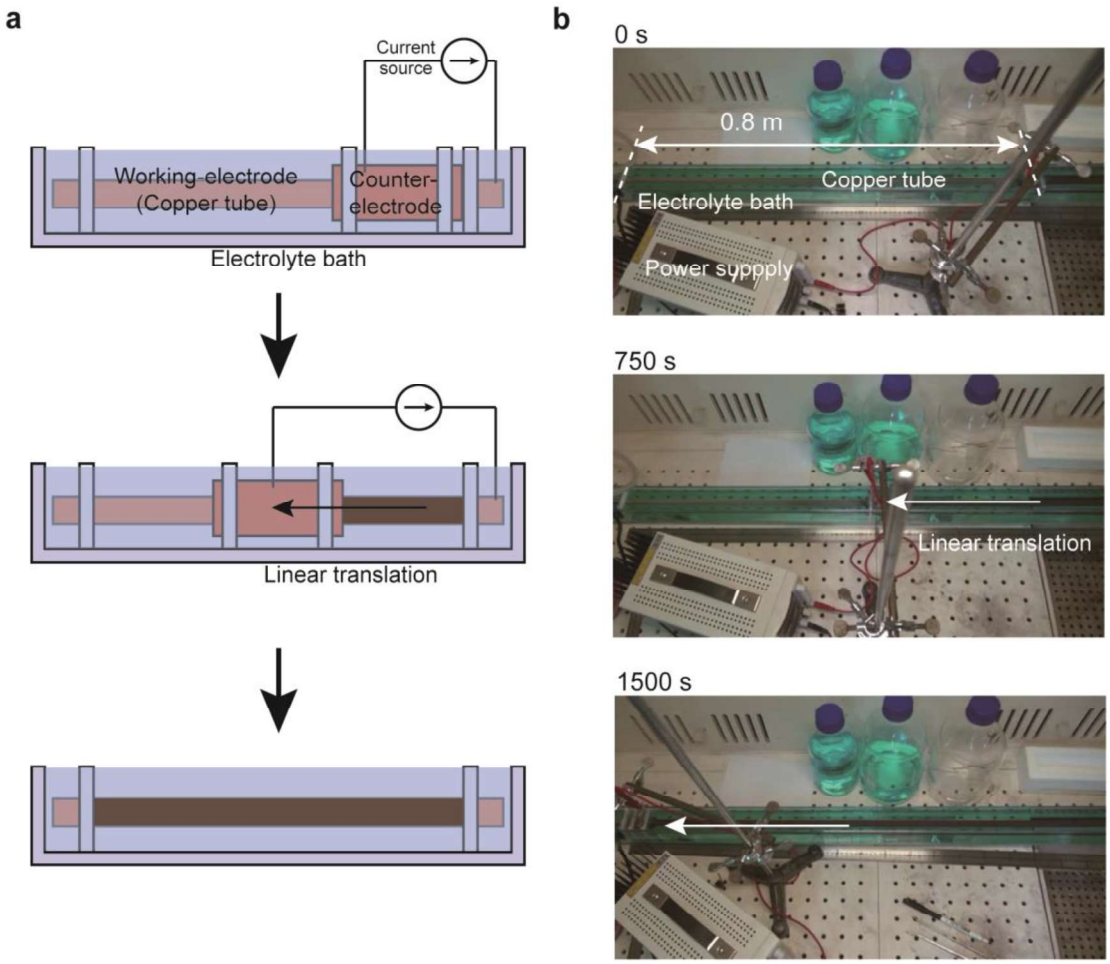

Figure S3. Continuous electrodeposition for meter-scale. (a) Schematic of the electrodeposition setup. (b) Sequential images of the continuous electrodeposition on a copper tube whose total length is 1 m.

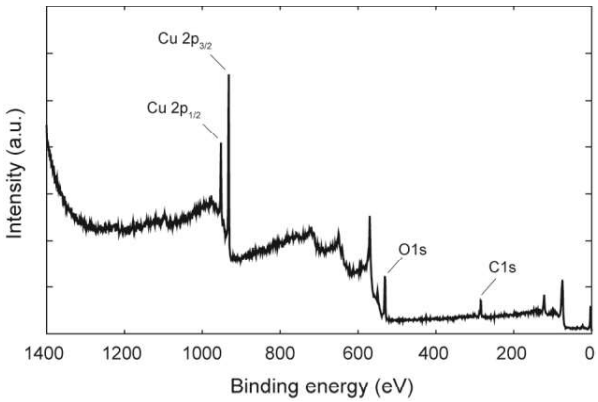

Figure S4. XPS spectra of the copper oxide dendrite sample. Porous structure prepared by electrodeposition in the surfactant-added electrolyte (3 mM) for 10 min. The signal of copper and oxygen indicates that the surface consists of copper oxide.

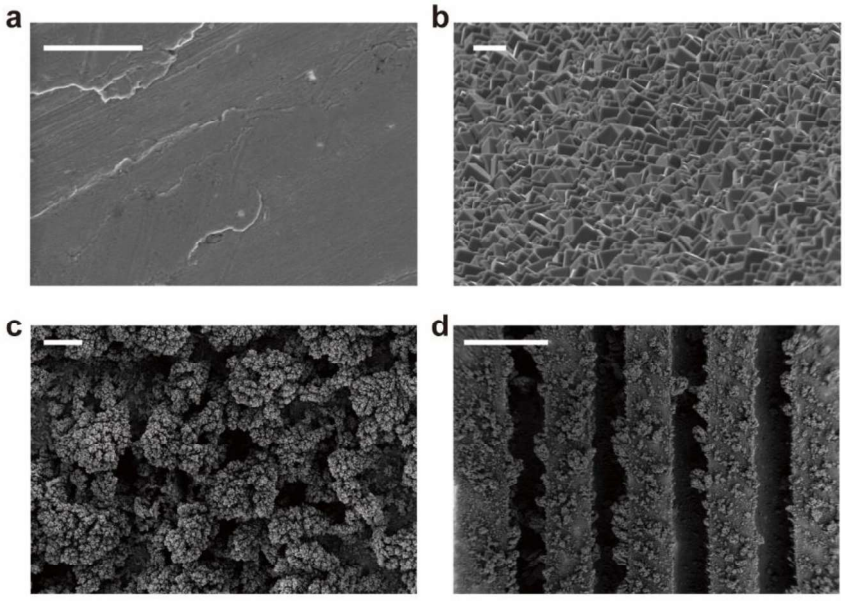

Figure S5. SEM images of copper surfaces with various treatment processes. (a) Pristine copper surface. (b) Cu_2O film *via* electroplating without hydrogen bubble generation. (c) Cu_2O porous structure *via* hydrogen bubble generation electroplating. (d) Cu_2O porous structure on rectangular grooves. Scale bar, 1 mm, 2 μm, 100 μm, 1 mm, from (a) to (d).

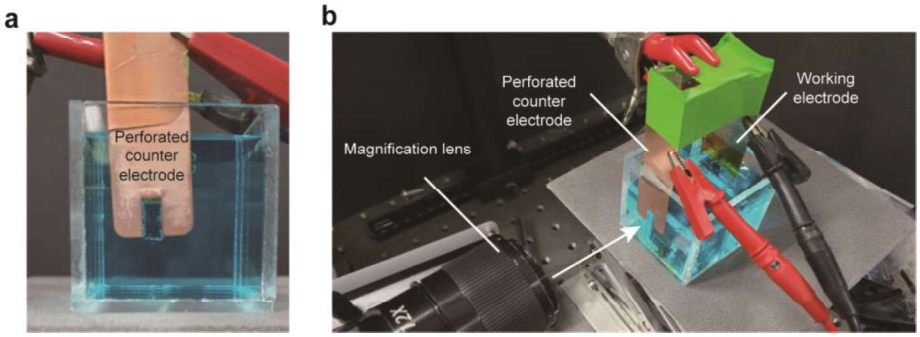

Figure S6. Bubble visualization setup. (a) Experimental setup showing the working electrode in front. In order to observe the hydrogen bubble generation on the surface in real time, the counter electrode was perforated as much as the plating area. (b) Bird-eye view of the experimental setup.

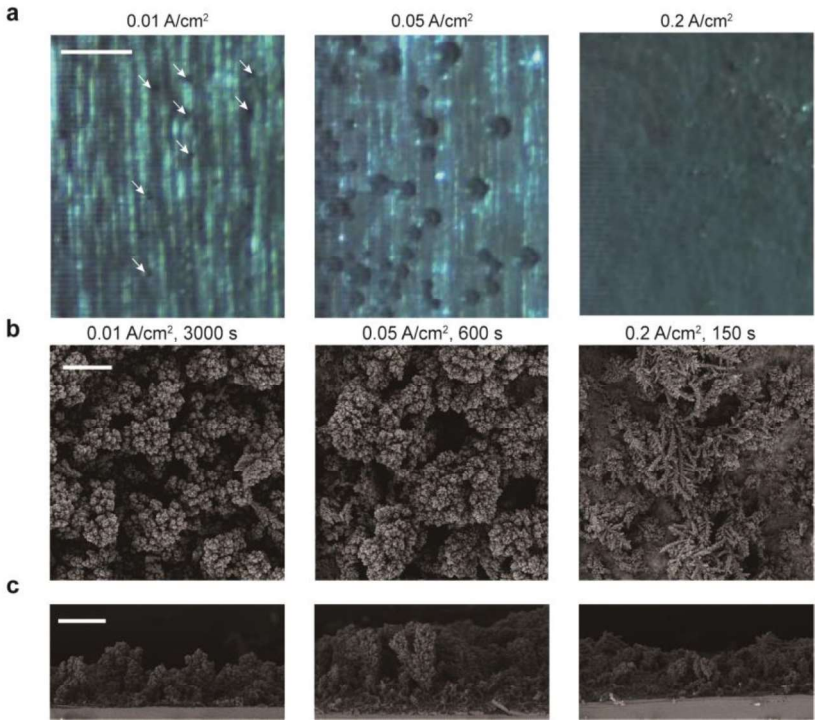

Figure S7. Effect of bubble generation on pore structure. (a) Visualization image of hydrogen bubble generation in real time. When the current density is 0.01 A·cm^{-2}, the bubbles are indicated by white arrows. Scale bar, 1 mm. (b) Top view SEM image of each sample after electroplating process. Scale bar, 100 μm. (c) The cross-sectional view of SEM image. Scale bar, 100 μm.

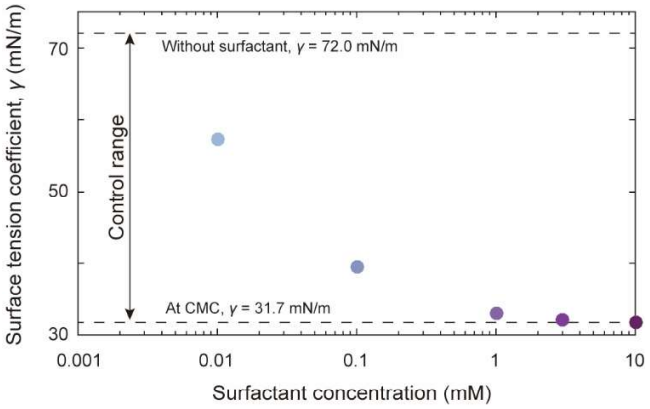

Figure S8. Surface tension coefficient of the electrolyte solution depending on the concentration of the added surfactant (SDS, sodium dodecyl sulfate). Our electrolyte solution commonly consists of 0.1 M CuSO4 and 0.5 M H_2SO_4, changing concentration of SDS to 0, 0.01, 0.1, 1, 3, 10 mM. In the absence of a surfactant, the surface tension coefficient is 72.0 mN/m, and as the concentration increases, the surface tension decreases. However, after reaching the CMC (Critical Micelle Concentration), at which the surfactant no longer affects interface and form micelles, the surface tension coefficient is relatively close to the constant (31.7 mN/m). We can control the surface tension of the electrolyte between 31.7 - 72.0 mN/m.

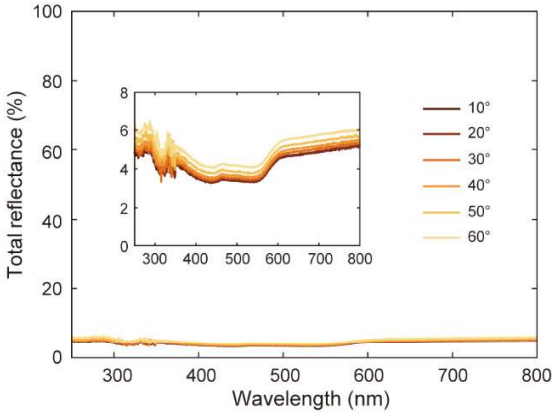

Figure S9. Total reflectance spectra for various incident angles using an integrating sphere. Total reflectance is near 4% at visible wavelength range, which implies an omnidirectional performance of copper oxide dendrites.

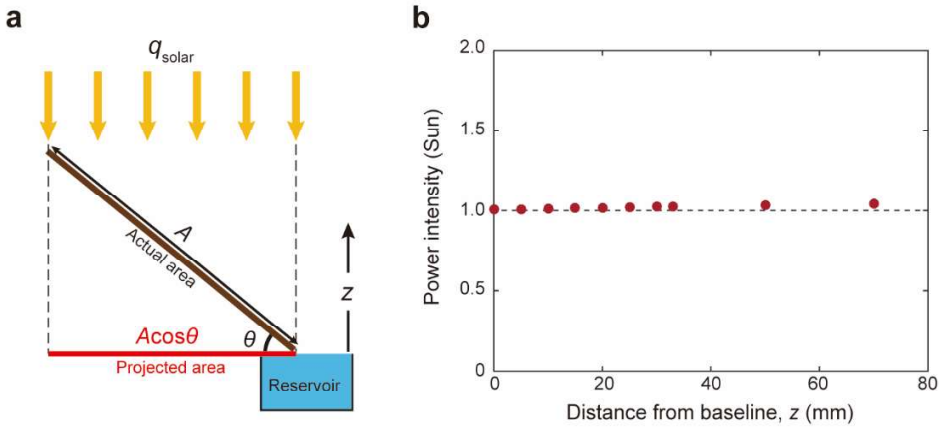

Figure S10. Schematic of the solar evaporation test and an illumination intensity profile. (a) The efficiency of solar evaporator ($\eta = \dot{m}_{\text{evap}} h_{fg} / [q_{\text{solar}}(Acos\theta)]$) is evaluated by the limited light projected area, $A\cos\theta$, while the actual area of the panel, A is fixed. (b) Solar simulator exhibiting an intensity change less than 4.15% for 7 cm distance from water interface(baseline), z.

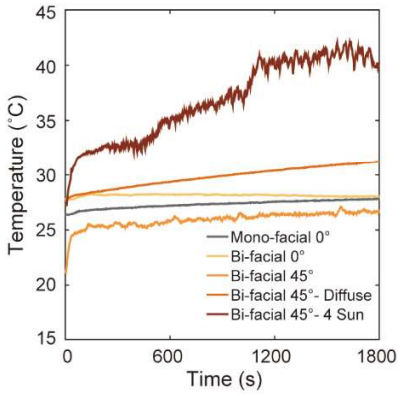

Figure S11. Temperature of reservoir vs evaporation time.

Supplementary Note 1. Evaporative capillary rise model and parameters

- Theoretical model for evaporative capillary rise in porous media

For predicting the dry-out of metre-scale solar evaporator, it is necessary to estimate the wet length. When capillary flow occurs along a porous material, the flow is limited by gravity and evaporation. In this model, we assume a one direction at flow that fully fills the cross-sectional area. For the control volume indicated as a red box in **Figure S2**, the inflow rate per unit width, Q_{in}, can be described as $Q_{\text{in}} = u(z)\tau$, where u(z), τ is respectively the flow velocity at the elevation z from the liquid interface of reservoir and the thickness of porous media. Then, considering the mass loss due to evaporation, the outflow rate per unit width, Q_{out} can be described as $Q_{\text{out}} = q_{\text{e}}(l - z) + \dot{l}\tau$, where q_{e}, l, and $\dot{l}$ is, respectively, the evaporation flux, the wet length, and the rate of rise. Here, the evaporation from the side is neglected, since the thickness of porous media is small compared to the width. The liquid rise velocity at point z is determined by equating Q_{in} and Q_{out} by the mass conservation, we write

$$u(z) = \dot{l} + \frac{q_{\text{e}} l}{\tau}\left(1 - \frac{z}{l}\right). \qquad \text{(S1)}$$

The capillary rise is driven by the pressure difference between the atmospheric pressure, p_{a} and the pressure inside liquid interface at the front of rise, $p_{\text{i}} = p_{\text{a}}\text{-}\gamma\kappa$. This pressure jump, which is called Laplace pressure, is proportional to surface tension coefficient, γ and the curvature of the interface, κ. The average flow velocity in porous media can be described by Darcy's law:

$$u(z) = -\frac{K}{\mu}\frac{\partial(p + \rho g z \sin\varphi)}{\partial z} \qquad \text{(S2)}$$

where K is the permeability of porous media, ρ the liquid density, μ the liquid viscosity, g the gravitational acceleration and φ the tilt angle of porous media.

Integrating Eq. (S2) with respect to z from 0 to l, we get the pressure balance equation between the Laplace pressure and the pressure drop due to gravitational and viscous resistance.

$$\frac{2\gamma}{r_{\mathrm{P}}} = \rho g l \sin\varphi + \frac{\mu}{K}\int_0^l u(z)dz. \qquad \text{(S3)}$$

Substituting **Equation S1** into **Equation S3**, we get a differential equation for l:

$$\dot{l} = \frac{a}{l} - b - cl,$$

Where $a = 2\gamma K/(r_{\mathrm{p}}\mu)$, $b = \rho g\sin\varphi/\mu$, $c = q_{\mathrm{e}}/(2\tau)$.

The maximum wet length correspond to the point where the front stops, $\dot{l} = 0$, then $l_{\mathrm{w,m}}$ is algebraically obtained as follows:

$$l_{\mathrm{w,m}} = -\frac{\rho g\sin\varphi\tau}{\mu q_{\mathrm{e}}} + \sqrt{\left(\frac{\rho g\sin\varphi\tau}{\mu q_{\mathrm{e}}}\right)^2 + \frac{4\gamma K\tau}{\mu r_p q_{\mathrm{e}}}}$$

In the case of horizontal plate, the equation is simplified to

$$l_{\mathrm{w,m}} = \sqrt{\frac{4\gamma K\tau}{\mu r_p q_{\mathrm{e}}}}$$

Table S1. Parameters for numerical simulation

Symbol	Description	Equation (or value)	Unit
K	Permeability	$K \approx \frac{4\varepsilon^3 r_p^2}{180(1-\varepsilon)^2}$	m^2
ε	Porosity	≈ 0.4 (Random packed beads)	-
q_{e}	Evaporation flux	0.789 - 100	$Kg/m^2/h$ (m/s)
τ	Thickness of porous media	0.0003	m
φ	Tilt angle of porous media	15, 30, 45, 90	°

Supplementary Note 2. Estimation of copper and copper oxide ratio

Since the average atomic ratio of copper and oxygen is 89.41 and 10.59% (averaged values after 600s in depth profile), respectively, the ratio of pure copper and copper oxide, x_{Cu} and x_{oxide} is calculated as follows.

$$x_{Cu} + 2\,x_{\text{oxide}} = 0.8941,$$

$$x_{\text{oxide}} = 0.1059.$$

The molar ratio of the copper and copper oxide is calculated as 6.45:1 (86.6:13.4). Therefore, the molar mass of deposited structure, M_s is 63.546 g/mol × 6.45/(6.45+1) + 143.09 g/mol × 1/(6.45+1) = 74.2 g/mol.

Supplementary Note 3. Comparison of capillary performance for estimation of wet length

Table S2. Comparison of capillary performance

Process type	Capillary performance K/r_p (μm)	Maximum wet length $l_{w,m}$ (m)	Process Time (min)	Area (cm^2)	Scalability ($cm^2 \cdot h^{-1}$)
Electrodeposition	0.395	0.139	50	17	20
	0.409	0.149	25	17	41
	0.464	0.193	10	17	102
	0.336	0.132	2.5	17	408
	0.244	0.036	1	17	1020
	0.200	0.023	0.5	17	2040
	0.790	0.369	30	17	34
Groove + Electrodeposition	6.200	1.035	10	17	102
Inverse opal[1, 2]	0.054	0.022	10	0.458	2.14
	0.005	0.007	12.8	0.458	1.37
	0.006	0.026	20	0.525	1.05
	0.027	0.054	30	0.525	0.52
	0.030	0.056	60	0.525	0.35
Mciropillar[3]	0.734	0.193	90	3.000	1.08
	1.005	0.303	166.5	3.000	0.67
	1.129	0.351	269.4	3.000	0.57
	1.168	0.378	313.2	3.000	0.52
Sintered wick[4-6]	0.194	0.359	346.7	8.100	4.05
	0.298	0.441	120	8.100	4.05
	0.472	0.604	120	8.100	4.05
	0.604	0.686	120	8.550	4.28
	0.154	0.335	120	10.000	5.00
	0.234	0.412	120	10.000	5.00
	0.596	0.659	120	10.000	5.00
	0.656	0.697	120	10.000	5.00

	0.448	0.571	120	10.000	5.00
	0.461	0.579	120	10.000	5.00
	0.761	0.744	120	10.000	5.00
	0.801	0.764	120	10.000	5.00
	0.479	0.591	120	10.000	5.00
	0.625	0.674	120	10.000	5.00
Sprayed porous wick[7]	0.001	0.011	120	12.000	6.00
	0.078	0.109	120	12.000	6.00
	0.134	0.141	120	12.000	6.00
	0.170	0.153	120	12.000	6.00
	0.243	0.161	120	12.000	6.00
	0.013	0.038	120	12.000	6.00
	0.109	0.146	120	12.000	6.00
	0.147	0.153	120	12.000	6.00
	0.194	0.159	120	12.000	6.00
	0.286	0.175	120	12.000	6.00
	0.145	0.160	120	12.000	6.00
	0.295	0.288	120	12.000	6.00
	0.368	0.297	120	12.000	6.00
	0.443	0.266	120	12.000	6.00
	0.443	0.219	120	12.000	6.00
CuNW array[8]	0.004	0.007	120	0.810	0.46
	0.010	0.011	105	0.810	0.46
	0.023	0.019	105	0.810	0.46
CuNW aerosponge[9]	0.228	0.397	105	1.661	0.83
	0.290	0.448	120	1.661	0.83

Supplementary Note 4. Optical absorption efficiency calculation

Optical absorption efficiency is the ratio of absorbed solar power density to actual provided solar power density. Integrating sphere UV-VIS-IR absorption data and Reference Air Mass 1.5 (AM 1.5G) solar spectra data provided from National Renewable Energy Laboratory (NREL) are used for calculation. Absorbed solar power density is multiplication of 1000.4 W/m^2 (1 Sun illumination) by sample's absorption ratio at 280 – 2700 nm wavelength region. The absorption ratio at 280 – 2700 nm wavelength is calculated by dividing absorbed solar power density by provided solar power density at 280 – 2700 nm. Absorbed solar power density at 280 – 2700 nm is calculated by integrating multiplication of absorption ratio by solar power density at each wavelength, from 280 to 2700 nm. Provided solar power density at 280 – 2700 nm is calculated to be 992.6 W/m^2, which is integration of solar spectra from 280 to 2700 nm. The actual provided solar power density is

multiplication of 1000.4 W/m^2 by factor of reduced area of normal plane to incident light due to tilted angle.

Supplementary Note 5. Physics of evaporation

The absolute value evaporation rate (Q_{evap}) can be quantified by the product of the mass transfer coefficient (h_{mass}), partial pressure difference of vapor between surface and the ambient air (Δp), and the area of the evaporation (A).[10]

$$Q_{\mathrm{evap}} = h_{\mathrm{mass}} \Delta p A_{\mathrm{evap}}$$

The areal evaporation rate (which is the evaporative rate in the paper) is normalized by the projection area ($A \cos\theta$), which can be expressed as below.

$$q_{\mathrm{evap}} = h_{\mathrm{mass}} \Delta p \cos^{-1}\theta$$

- Mass transfer coefficient

Founding on the similarity between the governing equation of mass transfer and heat transfer, the mass transfer coefficient is considered to be proportional to the heat transfer coefficient (h). Heat transfer coefficients on horizontal and inclined surfaces driven by natural convection are obtainable by experiment.

The experiment from previous study[11] reveals the experimental relationships between the natural convection coefficient and the buoyancy on horizontal or inclined plates.

For plates with horizontal arrangement, the experiment revealed the relationship below.

$$Nu_h = 0.16(Ra)^{0.33}$$

For plates with inclined arrangement, the experiment revealed the relationship.

$$Nu_i = 0.56(Ra\cos\theta)^{0.25}$$

Nu is the Nusselt number, which is the non-dimensionalized heat transfer coefficient. The index *h, i* represents horizontal and inclined arrangement, respectively. *Ra* is the Rayleigh number, which is the non-dimensionalized number indicating the relative intensity of natural convection. To be precise, the effect of vapor concentration on natural convection should be incorporated.[12] When vapor concentration increases, the gas density decreases because the molecular weight of water (~18) is lower than the average air (~29). Since higher temperature induces higher concentration of water vapor in the gas phase, the natural convection driven by increased vapor concentration facilitates the natural convection driven by increased temperature. However, in lower temperatures near ambient, the extent of concentration difference driven natural convection is minor compared to the temperature driven natural convection. Therefore, we only consider the effect of temperature difference on natural convection.

L is the length of the plate (or evaporator), k is the thermal conductivity of air, ρ is the density of air, β is the volumetric thermal expansion coefficient of air, g is the gravitational acceleration, ΔT is the temperature difference between surface and ambient air, μ is the dynamic viscosity of air, and α is the thermal diffusivity of air.

$$Nu = \frac{hL}{k}$$

$$Ra = \frac{\rho\beta g L^3 \Delta T}{\mu\alpha}$$

Disregarding the constant physical variables, the heat transfer coefficient can be represented by expressions in terms of length, temperature, and the angle of inclination. This uncomplicates examining and comparing the effects of temperature, length, and angle of inclination if the arrangement is fixed as horizontal or inclined arrangement. However, when comparing the horizontal arrangement versus the inclined arrangement, the simple proportional effect is not applicable since they are governed by different equations.

$$h_h \sim \Delta T^{0.33} L^0$$

$$h_i \sim \Delta T^{0.25} L^{-0.25} (\cos\theta)^{0.25}$$

Since the mass transfer coefficient is proportional to the heat transfer coefficient, the mass transfer coefficient has the same proportional relationship as the heat transfer coefficient.

$$h^h_{\text{mass}} \sim \Delta T^{0.33} L^0$$

$$h^i_{\text{mass}} \sim \Delta T^{0.25} L^{-0.25} (\cos\theta)^{0.25}$$

- Vapor pressure difference

The evaporation is driven by the difference between the partial pressure of vapor in the air adjacent to the surface and the ambient air. Here, we assume that the timescale of vapor diffusion is much longer than the timescale of molecular evaporation from liquid to adjacent air, indicating that the vapor pressure in the air adjacent near surface is assumed to be the saturated vapor pressure of the liquid.[13] The saturated vapor pressure has positive relations with temperature. Based on the balance of chemical potentials of the liquid and vapor phase, the Antoine equation quantifies the relationship between temperature and saturated vapor pressure.[14]

$$p_{\mathrm{sat}} = 10^{8.07-\frac{1731}{T/[^{\circ}\mathrm{C}]+233}}\ [\mathrm{mmHg}]$$

The absolute humidity of the ambient air as 0.50 where the ambient temperature was fixed at 21~22°C. Therefore, the vapor partial pressure of the ambient can be calculated. (The averaged value 21.5°C was used for the Antoine equation.)

$$p_{\mathrm{amb}} = 0.5 \times 10^{8.07-\frac{1731}{T_{amb}/[^{\circ}\mathrm{C}]+233}}\ [\mathrm{mmHg}] = 9.36$$

Therefore, the vapor pressure difference can be expressed as below.

$$\Delta p = 10^{8.07-\frac{1731}{T/[^{\circ}\mathrm{C}]+233}} - 9.36$$

- Area of evaporation

The bifacial evaporator has twice the evaporation area compared to the monofacial evaporator. We introduce the effective surface factor χ, which is the ratio of area covered with water to the monofacial area. Representing the monofacial area of evaporator as A, the evaporation area can be described as χA. For a fully wetted monofacial evaporator, the effective surface factor χ has the value of 1, and for a fully wetted bifacial evaporator, the factor χ has the value of 2. If the capillary strength is not high enough to wet the whole surface, the factor will have smaller values compared to the fully wetted case. Since the monofacial area A is proportional to the length L, the evaporation area is proportional with both L and χ.

$$A_{\mathrm{evap}} \sim \chi L$$

- Quantitative comparison

The absolute evaporation rate and the areal evaporation rate can be expressed in proportional expression.

$$Q_{\text{evap}} = h_{\text{mass}} \Delta p A_{\text{evap}}$$

$$q_{\text{evap}} = h_{\text{mass}} \Delta p (\cos\theta)^{-1}$$

Each terms of the equations may be substituted by their own proportional expression, resulting in new relations solely formulated in terms of temperature and length.

$$Q_{\text{evap},h} \sim \chi \Delta T^{0.33} L \left(10^{8.07 - \frac{1731}{T/[\text{°C}]+233}} - 9.36 \right)$$

$$Q_{\text{evap},i} \sim \chi \Delta T^{0.25} L^{0.75} (\cos\theta)^{0.25} \left(10^{8.07 - \frac{1731}{T/[\text{°C}]+233}} - 9.36 \right)$$

The areal evaporation rate can be expressed in a similar manner. Since the projected area for horizontal plate is always the same as its area, the cosine term is neglected in the equation for horizontal rate.

$$q_{\text{evap},h} \sim \chi \Delta T^{0.33} L^{0} \left(10^{8.07 - \frac{1731}{T/[\text{°C}]+233}} - 9.36 \right)$$

$$q_{\text{evap},i} \sim \chi \Delta T^{0.25} L^{-0.25} (\cos\theta)^{-0.75} \left(10^{8.07 - \frac{1731}{T/[\text{°C}]+233}} - 9.36 \right)$$

It is noticeable that temperature difference is the common factor in both cases. This agrees with the intuition: larger temperature difference results in larger density difference, which enhances the natural convection.

Length change is dependent only in inclined cases. This can be explained by the different configurations of the vapor stream that the ascends.

For the natural convection on horizontal plates, each stream of vapor directly ascends vertically, with weak interaction with the adjacent stream. Therefore, the length does not have a major impact on the convective mass transfer coefficient. However, when natural convection occurs on inclined plates, a boundary layer builds as the stream ascends. If the boundary layer gets larger, the spatial gradient of concentration decreases, yielding negative effects on mass transfer. Therefore, as the length increase, the evaporation per unit area decrease.

The positive effect of inclination angle is logical, since the gravitational acceleration is the driving force of buoyancy.

Supplementary Note 6. Heat and mass transfer analysis for solar interfacial evaporator

- Effect of effective surface area: monofacial-horizontal evaporator versus bifacial-horizontal evaporator

$$q_{\mathrm{evap},h} \sim \chi \Delta T^{0.33} L^{0} \left(10^{8.07 - \frac{1731}{T/[^{\circ}\mathrm{C}]+233}} - 9.36 \right)$$

The effect of effective surface area (χ) is examined by comparing the monofacial, horizontal evaporator versus the bifacial, horizontal evaporator. When comparing two horizontal evaporators, the simple proportional relation may be applicable. Each term in the proportional expression for the areal (normalized) evaporation rate is organized in the table below. The ambient temperature

was 22°C for monofacial evaporation experiment, and 21°C for bifacial experiment. The factor with the common value for (L) is neglected.

Table S3. Effect of effective surface area on surface temperature

	χ effective surface factor	T steady state tip temperature	ΔT temperature difference
Mono-facial	1	31 °C	9
Bi-facial	2	25 °C	4

The substituting the values, the quantitative assessment of areal evaporation rate becomes possible.

Table S4. Effect of effective surface area: monofacial-horizontal evaporator versus bifacial-horizontal evaporator

	Theoretical value (relative value)	Experimental value (in $\mathrm{kg/m^2}$)
Mono-facial	67.9	0.72
Bi-facial	73.2	0.86
Ratio (Mono/Bi)	0.93	0.83

The enhancement of evaporation due to bifacial evaporator is overestimated in the theoretical value by 12%. The effect of vapor concentration on natural convection and the edge effect due to the narrow geometry are regarded as the possible explanations for the deviation between our theory and the experimental value.

It is concludable that the effect of doubled area on total evaporation rate overcomes the combined effect of ①increased mass transfer coefficient (h_{mass}) due to increased temperature, ② increased concentration difference (Δc) due to increased temperature.

$$(h_{\mathrm{mass}}\Delta p)_{\mathrm{high}}A > (h_{\mathrm{mass}}\Delta p)_{\mathrm{low}}A \quad but \quad (h_{\mathrm{mass}}\Delta p)_{\mathrm{high}}A < (h_{\mathrm{mass}}\Delta p)_{\mathrm{low}}(2A)$$

- Effect of the inclination angle: bifacial-horizontal evaporator versus bifacial-inclined (45°) e vaporator

The effect of the inclination angle (θ) is examined by comparing the bifacial, horizontal evaporator versus the bifacial-inclined (45°) evaporator. When the evaporators with the different angle of inclination are in comparison, the simple proportional relationship does not hold. Therefore, calculations should be done with all the constants in account. The values from experiment are shown. The ambient temperature for both cases were 21 °C.

Table S5. Effect of the inclination angle on surface temperature

	T, steady state tip temperature	ΔT, temperature difference
0° (horizontal)	25 °C	4
45° (inclined)	27 °C	6

The calculation yields the result below.

Table S6. Effect of the inclination angle: bifacial-horizontal evaporator versus bifacial-inclined (45°) evaporator

	Theoretical value (relative value)	Experimental value (in $\mathrm{kg/m^2}$)
0° (horizontal)	1524	0.88
45° (inclined)	2460	1.44

Ratio (0^o / 45^o)	0.62	0.61

The estimation from the theoretical value gave great agreements with the experiment, presenting an error of 1%. Being similar to the first question, the effect of vapor concentration on natural convection and the edge effect due to the narrow geometry are regarded as the possible explanations for the deviation between our theory and the experimental value.

Supplementary Note 7. Feasibility test for the issue of salt accumulation issue in solar desalination

Solar interfacial evaporation is sustainable technology to water purification or desalination. However, in the case of desalination, the evaporator suffers salt accumulation issue. During the water evaporation, the solute remains, which causes salt to accumulate on porous structures and block the capillary path. The simple method to remove salt is washing or rinsing[15] which involve additional labor and cost. The most feasible solution for cleaning clogged surface with salt is a natural dissolution method using a day and night cycle.[16] Site-specific salt formation[17] is recently emerged to solving salt accumulation issue. The salt concentration increases to the terminus of evaporator as water evaporates, salt crystallization occurs only at the edge of evaporator while the main area of evaporator kept from salt accumulation.

In order to check how stable our device is from salt formation, we designed a simple accelerated cycle experiment device. Electroplated porous sample(P10) was oriented perpendicular to the simulated sea water (3.5 wt% NaCl) and contact with the liquid. Once the bottom edge of the sample touches the liquid surface, the liquid rises along the sample by capillary force. For accelerated cyclic test, heat equivalent to the solar irradiation per unit area per day (5 kWh/m^2) is

supplied through the ceramic heater attached to the back of the specimen for 6 minutes, and the power is turned off for the same period for cooling. As can be seen in **Figure S1a**, it was confirmed that salt continued to accumulate in the terminal except the main surface, even after about 60 cycles equivalent to 60 days (**Figure S1b)**. In addition, the accumulated salt can be simply dissolved in water and the sample is restored to initial state (**Figure S1c)**.

Supplementary Note 8. Cost estimation of the dendritic copper oxide wick and comparison

Table S7. Cost estimation of dendritic copper oxide wick and previous studies

Materials	**Material Consumption (per unit area)**	**Price**	**Price (per unit area)**
Cu plate (τ=0.25mm)	2.24 kg/m^2	4.0 $/kg	9.0 $/m^2
$CuSO_4$ (for electrolyte)	1.55 mol/m^2	2.4 $/mol	3.7 $/m^2
Sulfuric acid (for electrolyte)	855 ml/m^2	0.0018 $/ml	1.5 $/m^2
Cost of our device			**14 $/m^2**

Cost ($/m^2)	**Materials**
14	**Dendritic Cu oxide**
39	Geopolymer-Mesoporous Carbon composites[18]
567	MoS2/C @ PU composite[19]
18	PPy Origami(artificial rose)[20]
3	Graphite-coated wood[21]

Supplementary Note 9. Comparison of evaporation performance

Table S8. Evaporation rates and absorber materials of previous studies

	Evaporation rate (kg m^{-2} h^{-1})	**Absorber material**
This work	1.76	Copper oxide
Carbonized mushrooms[22]	1.475	Carbonaceous material
Hierarchical foam of graphene[23]	1.33	Carbonaceous material
Graphite-coated wood[21]	0.9	Carbonaceous material

Natural wood with carbonized surface[24]	0.82	Carbonaceous material
Ti_2O_3 NPs[25]	1.32	Semiconductor
Gold film and NPs[26]	0.96	Plasmonic particle
AlO_3 on copper foam[27]	1.39	Semiconductor
MOF on Cu mesh[28]	1.2	Hybrid
PVA-PPy hydrogel[29]	3.2	Polymer

REFERENCES

(1) Zhang, S.; Lin, L.; Chen, G.; Tang, H.; Zeng, J.; Yuan, W.; Tang, Y., Experimental Study on the Capillary Performance of Aluminum Micro-Grooved Wicks with Reentrant Cavity Array. *Int. J. Heat Mass Transfer* **2019**, *139*, 917-927.

(2) Zhang, C.; Lingamneni, S.; Barako, M. T.; Palko, J. W.; Asheghi, M.; Goodson, K. E. *In Characterization of The Capillary Performance of Copper Inverse Opals*, 2016 15th IEEE Intersociety Conference on Thermal and Thermomechanical Phenomena in Electronic Systems (ITherm), 31 May-3 June 2016; **2016**; pp 1035-1039.

(3) Nam, Y.; Sharratt, S.; Byon, C.; Kim, S. J.; Ju, Y. S., Fabrication and Characterization of the Capillary Performance of Superhydrophilic Cu Micropost Arrays. *J Microelectromech Syst* **2010**, *19* (3), 581-588.

(4) Deng, D.; Liang, D.; Tang, Y.; Peng, J.; Han, X.; Pan, M., Evaluation of Capillary Performance of Sintered Porous Wicks for Loop Heat Pipe. *Exp. Therm Fluid Sci.* **2013**, *50*, 1-9.

(5) Deng, D.; Tang, Y.; Huang, G.; Lu, L.; Yuan, D., Characterization of Capillary Performance of Composite Wicks for Two-Phase Heat Transfer Devices. *Int. J. Heat Mass Transfer* **2013**, *56* (1), 283-293.

(6) Holley, B.; Faghri, A., Permeability and Effective Pore Radius Measurements for Heat Pipe and Fuel Cell Applications. *Appl. Therm. Eng.* **2006**, *26* (4), 448-462.

(7) Feng, C.; Yugeswaran, S.; Chandra, S., Capillary Rise of Liquids in Thermally Sprayed Porous Copper Wicks. *Exp. Therm Fluid Sci.* **2018**, 98, 206-216.

(8) Lee, J.; Suh, Y.; Dubey, P. P.; Barako, M. T.; Won, Y., Capillary Wicking in Hierarchically Textured Copper Nanowire Arrays. *ACS Appl. Mater. Interfaces* **2019**, *11* (1), 1546-1554.

(9) Jung, S. M.; Preston, D. J.; Jung, H. Y.; Deng, Z.; Wang, E. N.; Kong, J., Porous Cu Nanowire Aerosponges from One-Step Assembly and their Applications in Heat Dissipation. *Adv. Mater.* **2016**, *28* (7), 1413-1419.

(10) Welty, J.; Rorrer, G. L.; Foster, D. G., *Fundamentals of momentum, heat, and mass transfer*. John Wiley & Sons: 2020.

(11) Fujii, T.; Imura, H., Natural-Convection Heat Transfer From a Plate with Arbitrary Inclination. *Int. J. Heat Mass Transfer* **1972,** *15* (4), 755-767.

(12) Gebhart, B.; Pera, L., The Nature of Vertical Natural Convection Flows Resulting from the Combined Buoyancy Effects of Thermal and Mass Diffusion. *Int. J. Heat Mass Transfer* **1971,** *14* (12), 2025-2050.

(13) Sáenz, P. J.; Wray, A. W.; Che, Z.; Matar, O. K.; Valluri, P.; Kim, J.; Sefiane, K., Dynamics and Universal Scaling Law in Geometrically-Controlled Sessile Drop Evaporation. *Nat. Commun.* **2017,** *8* (1), 14783.

(14) Reid, R. C.; Prausnitz, J. M.; Sherwood, T. K., *The Properties of Liquids and Gases.(Stichworte Teil 2)*. McGraw-Hill: 1977.

(15) Zhu, B.; Kou, H.; Liu, Z.; Wang, Z.; Macharia, D. K.; Zhu, M.; Wu, B.; Liu, X.; Chen, Z., Flexible and Washable CNT-Embedded PAN Nonwoven Fabrics for Solar-Enabled Evaporation and Desalination of Seawater. *ACS Appl. Mater. Interfaces* **2019,** *11* (38), 35005-35014.

(16) Zhu, M.; Li, Y.; Chen, F.; Zhu, X.; Dai, J.; Li, Y.; Yang, Z.; Yan, X.; Song, J.; Wang, Y.; Hitz, E.; Luo, W.; Lu, M.; Yang, B.; Hu, L., Plasmonic Wood for High-Efficiency Solar Steam Generation. *Adv. Energy Mater.* **2018,** *8* (4), 1701028.

(17) Xia, Y.; Hou, Q.; Jubaer, H.; Li, Y.; Kang, Y.; Yuan, S.; Liu, H.; Woo, M. W.; Zhang, L.; Gao, L.; Wang, H.; Zhang, X., Spatially Isolating Salt Crystallisation from Water Evaporation for Continuous Solar Steam Generation and Salt Harvesting. *Energy Environ. Sci.* **2019,** *12* (6), 1840-1847.

(18) Liu, F.; Zhao, B.; Wu, W.; Yang, H.; Ning, Y.; Lai, Y.; Bradley, R., Low Cost, Robust, Environmentally Friendly Geopolymer–Mesoporous Carbon Composites for Efficient Solar Powered Steam Generation. *Adv. Funct. Mater.* **2018,** *28* (47), 1803266.

(19) Li, W.; Tekell, M. C.; Huang, Y.; Bertelsmann, K.; Lau, M.; Fan, D., Synergistic High-Rate Solar Steaming and Mercury Removal with MoS2/C @ Polyurethane Composite Sponges. *Adv. Energy Mater.* **2018,** *8* (32), 1802108.

(20) Li, W.; Li, Z.; Bertelsmann, K.; Fan, D. E., Portable Low-Pressure Solar Steaming-Collection Unisystem with Polypyrrole Origamis. *Adv. Mater.* **2019,** *31* (29), 1900720.

(21) Li, T.; Liu, H.; Zhao, X.; Chen, G.; Dai, J.; Pastel, G.; Jia, C.; Chen, C.; Hitz, E.; Siddhartha, D.; Yang, R.; Hu, L., Scalable and Highly Efficient Mesoporous Wood-Based Solar Steam Generation Device: Localized Heat,

Rapid Water Transport. *Adv. Funct. Mater.* **2018,** *28* (16), 1707134.

(22) Xu, N.; Hu, X.; Xu, W.; Li, X.; Zhou, L.; Zhu, S.; Zhu, J., Mushrooms as Efficient Solar Steam-Generation Devices. *Adv. Mater.* **2017,** *29* (28), 1606762.

(23) Ren, H.; Tang, M.; Guan, B.; Wang, K.; Yang, J.; Wang, F.; Wang, M.; Shan, J.; Chen, Z.; Wei, D.; Peng, H.; Liu, Z., Hierarchical Graphene Foam for Efficient Omnidirectional Solar–Thermal Energy Conversion. *Adv. Mater.* **2017,** *29* (38), 1702590.

(24) Zhu, M.; Li, Y.; Chen, G.; Jiang, F.; Yang, Z.; Luo, X.; Wang, Y.; Lacey, S. D.; Dai, J.; Wang, C.; Jia, C.; Wan, J.; Yao, Y.; Gong, A.; Yang, B.; Yu, Z.; Das, S.; Hu, L., Tree-Inspired Design for High-Efficiency Water Extraction. *Adv. Mater.* **2017,** *29* (44), 1704107.

(25) Wang, J.; Li, Y.; Deng, L.; Wei, N.; Weng, Y.; Dong, S.; Qi, D.; Qiu, J.; Chen, X.; Wu, T., High-Performance Photothermal Conversion of Narrow-Bandgap Ti2O3 Nanoparticles. *Adv. Mater.* **2017,** *29* (3), 1603730.

(26) Zhou, L.; Tan, Y.; Ji, D.; Zhu, B.; Zhang, P.; Xu, J.; Gan, Q.; Yu, Z.; Zhu, J., Self-Assembly of Highly Efficient, Broadband Plasmonic Absorbers for Solar Steam Generation. *Sci. Adv.* **2016,** *2* (4), e1501227.

(27) Xu, N.; Li, J.; Wang, Y.; Fang, C.; Li, X.; Wang, Y.; Zhou, L.; Zhu, B.; Wu, Z.; Zhu, S., A Water Lily–Inspired Hierarchical Design for Stable and Efficient Solar Evaporation of High-Salinity Brine. *Sci. Adv.* **2019,** *5* (7), eaaw7013.

(28) Ma, Q.; Yin, P.; Zhao, M.; Luo, Z.; Huang, Y.; He, Q.; Yu, Y.; Liu, Z.; Hu, Z.; Chen, B.; Zhang, H., MOF-Based Hierarchical Structures for Solar-Thermal Clean Water Production. *Adv. Mater.* **2019,** *31* (17), 1808249.

(29) Zhao, F.; Zhou, X.; Shi, Y.; Qian, X.; Alexander, M.; Zhao, X.; Mendez, S.; Yang, R.; Qu, L.; Yu, G., Highly Efficient Solar Vapour Generation via Hierarchically Nanostructured Gels. *Nat. Nanotechnol.* **2018,** *13* (6), 489-495.